POLITECNICO DI TORINO
Repository ISTITUZIONALE

Design and Testing of a Laser-Based Wireless Power Transmission Subsystem for Lunar Satellite Constellations

Original
Design and Testing of a Laser-Based Wireless Power Transmission Subsystem for Lunar Satellite Constellations / Sfasciamuro, Mr.D.E., Matonti, C.L., Lopez, F., Mauro, A., Mauro, S., Villa, A.. - In: AEROSPACE SCIENCE AND TECHNOLOGY. - ISSN 1270-9638. - ELETTRONICO. - 179, Part 1:(2026). [10.1016/j.ast.2026.113219]

Availability:
This version is available at: 11583/3013601 since: 2026-07-27T19:21:14Z

Publisher:
Elsevier

Published
DOI:10.1016/j.ast.2026.113219

Terms of use:

This article is made available under terms and conditions as specified in the corresponding bibliographic description in the repository

Publisher copyright

(Article begins on next page)

20 November 2026

Aerospace Science and Technology 179 (2026) 113219

Contents lists available at ScienceDirect

Aerospace Science and Technology

journal homepage: www.elsevier.com/locate/aescte

Original article

Design and testing of a laser-based wireless power transmission subsystem for lunar satellite constellations

Domenico Edoardo Sfasciamuro [a,*], Catello Leonardo Matonti [a,*], Francesco Lopez [b], Anna Mauro [c], Stefano Mauro [a], Andrea Villa [d]

[a] Department of Mechanical and Aerospace Engineering, Politecnico di Torino, Turin, 10129, Italy
[b] Department of Energy, Politecnico di Torino, Turin, 10129, Italy
[c] Department of Electronics and Telecommunications, Politecnico di Torino, Turin, 10129, Italy
[d] ORiS S.r.l., Corso Castelfidardo 30/A, Turin, 10129, Italy

ARTICLE INFO

Communicated by Dr Mehdi Ghoreyshi

PACS:
45.50.Pk
J0101

2000 MSC:
70F05

Keywords:
Design
Testing
Lunar space-based solar power
Wireless power transmission
Laser

ABSTRACT

This study presents the design and preliminary verification of a wireless power transmission (WPT) system based on high-power laser emission from lunar orbit. The system comprises a constellation of satellites in quasi-frozen lunar orbits, equipped with high-efficiency fiber lasers that convert solar energy into optical power. This energy is beamed to the Moon's surface, where it is received and converted into electricity by photonic power converters (PPCs) located near strategic infrastructure zones. The paper focuses on key subsystems relevant to satellite design and testing, including laser payload integration, beam collimation optics, thermal management, and pointing accuracy control using Fine Steering Mirrors. A full satellite model is dimensioned, and its inertia matrix is derived to support attitude control design under realistic external disturbances such as solar radiation pressure and the lunar gravity gradient. Experimental validation of PPC performance under different laser power densities is conducted to assess efficiency and thermal behavior. Results confirm the feasibility of laser WPT for lunar environments and provide critical input for subsystem qualification and mission planning. The study advances the design and subsystem-level testing of satellite-based laser WPT architectures for lunar power stations, with a focus on orbital dynamics, laser integration, thermal management, beam steering, and power conversion.

1. Introduction

The New Space Race is going to bring back a number of missions to the lunar surface: according to ESA, more than 100 lunar missions, by private companies and government entities, are expected to take place by 2030 [1]. From the years of the first Space Race, space exploration has shifted from a competition between a few superpowers to an unprecedented level of global collaboration between a number of countries and private entities. India and Japan recently became the fourth and fifth nations to attempt soft landings on the Moon [2,3], joining the United States, Russia and China among lunar-capable spacefaring nations. While Japan's SLIM mission experienced an anomalous landing configuration due to an engine failure during descent, it successfully demonstrated high-precision landing capabilities and returned valuable scientific and engineering data. Plans have been made for robotic exploration and in situ resource utilization (ISRU), as well as construction of infrastructure to allow long-term human space habitation. These new mission concepts demand not only innovative solutions, but also a reliable design, testing and verification process for each spacecraft subsystem involved. India's Chandrayaan-3 achieved the first soft landing in the vicinity of the lunar South Pole, while Intuitive Machines' IM-1 mission marked the first commercial lunar landing attempt. Although IM-1 landed in a non-nominal attitude following a landing gear anomaly, the lander remained partially operational and successfully transmitted data back to Earth, representing a significant milestone for commercial lunar exploration. The Indian Space Research Organisation (ISRO) and the Japan Aerospace Exploration Agency (JAXA) have planned a joint lunar mission to send an uncrewed lunar lander to explore the south pole region no earlier than 2026 [4]. The China National Space Administration (CNSA) and Roscosmos plan to build an International Lunar Research Station (ILRS) on the lunar surface by 2030 [5].

In addition to the extreme conditions of the lunar environment, e.g. in terms of temperature and radiation, the lighting conditions at the south pole of the Moon are unique. The mean inclination of the lunar

* Corresponding authors.
E-mail addresses: domenico.sfasciamuro@polito.it (D.E. Sfasciamuro), catello.matonti@polito.it (C.L. Matonti), francesco.lopez@polito.it (F. Lopez), anna.mauro@polito.it (A. Mauro), stefano.mauro@polito.it (S. Mauro), a.villa@oris-space.com (A. Villa).

https://doi.org/10.1016/j.ast.2026.113219
Received 3 September 2025; Received in revised form 2 April 2026; Accepted 13 July 2026
Available online 27 July 2026
1270-9638/© 2026 The Author(s). Published by Elsevier Masson SAS. This is an open access article under the CC BY license (http://creativecommons.org/licenses/by/4.0/).

orbit with respect to the ecliptic plane is 1.5[°]. Due to this, at the poles the Sun never rises more than a few degrees above the horizon. Combined with the topography of the lunar surface, the high mountain peaks and deep craters create many Permanently Shadowed Regions (PSRs) where solar panels cannot be used to generate electricity [6]. Setting up new activities and planning to stay for much longer periods of time will require more powerful and reliable energy resources. On the Moon, the alternation between light and shadow is far more extreme than on Earth or even Mars. Due to the lack of atmosphere, obstacles cast extremely long and rapidly moving shadows. Solar-powered rovers have to pull out from these areas of extreme darkness while sampling the territory around themselves and maintaining communications with Earth. During long periods of darkness, the rovers must inevitably park in identified safe areas at higher elevations [7,8]. All these requirements extremely complicate a mission, increasing costs and risks.

One of the main solutions investigated for the Moon is Wireless Power Transmission (WPT) [9,10]. This theme has gained significant momentum in recent years, driven by advancements in technology and the growing need for efficient and flexible energy solutions. WPT is increasingly being applied in various sectors [11–13], including electric vehicle charging, consumer electronics, and industrial automation. In space, WPT is explored as a viable method for powering satellites, rovers, and lunar bases, where traditional energy sources are limited. The Italian start-up ORiS (Orbital Recharge in Space), a spin-off of the Politecnico di Torino, has been studying and developing Wireless Power Transmission in Space for years, particularly for lunar applications [14,15]. The company is conducting several experimental activities and collaborative efforts aimed at demonstrating the technological readiness of WPT subsystems in relevant operational conditions.

This paper presents the solution to the challenge of lunar power supply using WPT. An architecture has been developed based on a constellation of satellites in advantageous lunar orbits, such as quasi-frozen orbits, which almost continuously store solar energy onboard and then transmit it to the lunar surface via a high-power laser beam. On the lunar surface, specially designed receivers are strategically placed near locations of scientific and economic interest. This system enables energy generation directly at the site of use, effectively addressing or mitigating the challenges posed by long lunar nights and the shadows cast by the Moon's unique terrain. In addition, this technology can sustain high power peaks, complementing traditional solar energy systems. The key subsystems are the satellite-mounted laser, the targeting mechanism, the thermal management system, and the lunar receiver. This paper provides a detailed analysis of some of these subsystems, with emphasis on early-stage design activities, experimental testing, and their integration within the broader system. This study primarily focuses on the definition of the overall system architecture and the preliminary design of an innovative satellite capable of transmitting kilowatts of optical power over hundreds of kilometers. The laser and receiver systems are discussed in detail, and the transmitting satellite is sized with particular attention to the management of low-frequency disturbances. The performance of the pointing system, featuring Fine Steering Mirror (FSM) technology, is also assessed to ensure sub-arcsecond accuracy from orbit to the lunar surface.

In Section 2 the architecture designed and developed for the WPT system is briefly described with a reference to the requirements and characteristics of different subsystem. In Section 3 the focus is on the high-power laser system to be mounted onboard the satellites. Starting from the system-level requirements, various characteristics of the payload are analyzed. In Section 4, a preliminary satellite sizing is provided, along with a CAD model from which inertia characteristics are extrapolated. In Section 5 the orbital and pointing requirements are analyzed and a preliminary design of the satellite is presented and subsequently in Section 6 the gravity gradient and solar radiation pressure acting as external disturbances on the satellite are examined and calculated. Lastly, in Section 7, the rotational actuator system is sized to effectively mitigate the disturbances caused by solar radiation pressure and gravity gradient forces acting on the large-area spacecraft. Finally, in Section 8 the receiver placed on the lunar surface is studied in terms of material choice, optical-to-electric efficiency, and thermal behavior, including laboratory tests on photovoltaic cells designed for monochromatic radiation.

2. Lunar WPT architecture

The solution explored in this work, consists of a constellation of satellites in lunar orbit tasked with collecting solar energy using large arrays of solar panels. This energy is converted into optical power using a laser source and transmitted to the lunar surface via the laser beam. The optical power arriving on the lunar surface is then reconverted into electrical power using photovoltaic panels called Photonic Power Converters (PPC) [16,17] and stored in dedicated batteries if necessary. The satellite's main subsystems cited before are the pointing system, thermal system and integration of the laser system in space, as well as the receiver architecture. Specifically, the laser used is a collimated, high-efficiency fiber laser emitting at 1064 [nm] with efficiency approaching 40%. This choice of laser minimizes transmission losses. To achieve a manageable beam size on the lunar surface and ensure its effectiveness for power harvesting, proper beam expansion and collimation at the source are necessary, using optical chains of lenses or mirrors. Of the two solutions, metallic mirrors are preferred mainly because they are easier to cool with a thermal management system. Parabolic metallic mirrors can create an off-axis telescope with optical coatings optimized for visible and near-infrared wavelengths, avoiding chromatic and spherical aberration common in optical telescopes. Numerous methods exist for combining laser beams, each with varying suitability for specific applications. Another fundamental system for transmission is, of course, the pointing mechanism. Given lunar orbits at altitudes of hundreds of kilometers, precision close to a tenth of an arcsecond is required as explained in Section 5.1. To achieve this and prevent vibrational disturbances from the satellite and orbital movements from hindering transmission, the pointing system is divided into three levels. Firstly, the satellite's Guidance, Navigation, and Control system (GNC); secondly, a two-axis gimbal rotation system; and finally, Fine Steering Mirrors (FSM) mounted on the gimbal and controlled by piezoelectric actuators, allowing the beam to be directed with absolute precision. Lastly, the thermal management of the satellite, especially of the high-power laser and the receiver on the lunar surface, is of critical importance. Several tests have been conducted to study the response of the receiver cells to different laser power levels and to characterize them.

2.1. Orbit and operational geometry

The proposed Wireless Power Transmission (WPT) architecture is based on a constellation of satellites operating in lunar orbit, with a specific interest in quasi-frozen orbital configurations. Such orbits exploit the lunar gravity field and third-body perturbations to maintain quasi-constant orbital elements, thereby improving mission efficiency and simplifying long-term operations.

For the preliminary pointing, illumination, and attitude analyses developed in this work, a representative circular lunar orbit at an altitude of approximately $h \sim 600$ [km] is assumed. The satellite motion is modeled using a two-body approximation, starting from the following orbital parameters: semi-major axis $a = 4337.4$ [km], eccentricity $e = 0$, inclination $i = 89[°]$, argument of perigee $\omega = 90[°]$, and mean anomaly $M = 0[°]$ at the reference epoch of January 1, 2000, 12:00 TDB. The Right Ascension of the Ascending Node (RAAN) is treated as a free parameter and varied to investigate its impact on the Sun-spacecraft geometry.

At this orbital altitude, the satellite-to-surface link length is of the order of several hundred kilometers, requiring sub-arcsecond (microradian-class) pointing accuracy to constrain the linear displacement of the laser spot at the receiver to the meter scale. The transmission

Table 1
Summary of the reference mission-level specifications adopted for the lunar wireless power transmission architecture.

Parameter	Value	Note
Mission concept	Laser WPT from lunar orbit to surface	Reference architecture
Reference orbit type	Quasi-frozen / circular preliminary case	Simplified two-body analysis
Reference orbit altitude	~600 [km]	Baseline for pointing and transmission analysis
Receiver location	Lunar south pole, near Shackleton crater	Representative strategic site
Laser wavelength	1064 [nm]	Fiber laser baseline
Spacecraft solar array area	~21 $[m]^2$	Preliminary sizing value
Spacecraft mass	600 [kg]	CAD-based preliminary design
Target beam spot diameter on surface	≤10 [m]	Receiver-compatible footprint
Required pointing accuracy	Microradian class	To limit surface error to meter scale
Receiver technology	PPC for 1064 [nm]	Monochromatic optical-to-electrical conversion
Measured PPC efficiency in this work	14.6–16.3%	Best laboratory results obtained in this study
Transmission duration in cone	~1123 [s]	Reference case with $\theta_{max} = 60$ [°]

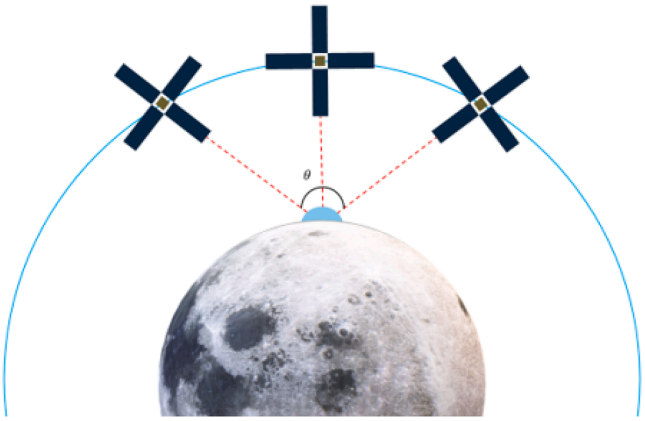


Fig. 1. Orbital transmission architecture.

geometry is analyzed assuming a fixed ground receiver located at the lunar South Pole, close to the Shackleton crater, a site of high interest for sustained surface operations.

Fig. 1 illustrates a preliminary configuration of the laser power transmission from lunar orbit to the surface. A key parameter governing the transmission performance is the beam divergence angle θ, whose role is discussed in detail in Section 5.1. The relative Sun-spacecraft geometry, which directly affects both thermal and power generation aspects, is evaluated as a function of time using lunar ephemerides from the JPL HORIZONS system, considering worst-case illumination conditions associated with specific RAAN values.

2.2. Power generation and conversion chain

Each transmitting spacecraft collects solar energy via large-area solar arrays. A representative sizing, as shown in [14], used in the present satellite model assumes a total solar array area on the order of $A_{SA} \approx 21$ $[m^2]$; this can be seen as the minimum size required to allow the battery pack to recharge during orbit and power the laser during the transmission cone. To avoid an excessively heavy battery pack, during transmissions with the satellite exposed to the Sun, the laser will be powered simultaneously by batteries and solar panels, significantly increasing the size of the solar panels. As for transmissions in shadow, the EPS system will be sized to power the laser at a percentage of its total power. The electrical energy produced is stored on-board and then converted to optical power by the laser payload. High-level efficiency contributions can be summarized as follows: (i) solar-to-electrical conversion on the spacecraft, assumed to be approximately 30% for state-of-the-art solar cells; (ii) electro-optical conversion in the laser payload, assumed to be approximately 40% for modern ytterbium-doped fiber laser architectures; and (iii) optical-to-electrical conversion on the lunar surface, which for receiver technologies compatible with $\lambda \approx 1064$ [nm] can be in the range of 35%–40% under representative operating conditions.

This chain provides an effective figure of merit for the end-to-end architecture, corresponding to an overall available power on the order of 165 [W] per unit solar array area (i.e., 165 $[W/m^2]$ of spacecraft solar arrays) when accounting for the above conversion stages. This value is used throughout the paper as a system-level reference to link spacecraft sizing to delivered optical/electrical power. To improve the readability of the proposed architecture and provide a concise overview of the reference mission scenario, the main mission-level specifications adopted throughout this work are summarized in Table 1. These parameters define the baseline case used for the preliminary orbital, power, pointing, and receiver analyses presented in the following sections.

The values reported in Table 1 define the reference configuration used in the remainder of the paper. In particular, the selected orbital altitude and receiver location establish the transmission geometry, while the laser wavelength, spacecraft size, and target beam footprint drive the sizing of the optical payload and the pointing requirements. The table also highlights the current experimental performance of the receiver technology, thereby linking the mission architecture to the laboratory validation activities discussed in Section 8.

2.3. Laser payload, optical output, and emission aperture

Power transmission is performed using a continuous-wave (CW) near-infrared laser source, in particular the high-efficiency fiber laser due to its superior beam quality, compactness, and scalability to multi-kilowatt output power. To deliver these levels of optical power from lunar orbit while limiting diffraction-driven spreading, beam expansion and collimation are required at the source through a dedicated optical chain.

Reflective optics (i.e., metallic mirror-based solutions) are favored for high-power handling and thermal management. The effective emission aperture is driven by the selected beam waist and the requirement to constrain the far-field spot size on the lunar surface to a receiver-compatible footprint. In the baseline architecture discussed in this work, the beam waist is selected in the range of a few tens of centimeters (representative optimum values are discussed later), corresponding to an emission aperture scale on the same order of magnitude.

2.4. Ground beam footprint and receivers distribution

Even in vacuum propagation, diffraction determines the evolution of the beam radius with distance. Under a Gaussian-beam assumption, the beam footprint on the lunar surface can be controlled by selecting the beam waist and by preserving high beam quality (i.e., low M^2). For transmission distances of several hundred kilometers and beam waist radii in the decimeter range, the resulting spot diameter can be kept within approximately 10 m, which is a practical upper bound for receiver deployment and for managing power density and thermal loads.

Beam quality strongly affects the achievable footprint at a given distance: lower-quality beams (higher M^2) require larger emission apertures (larger beam waist) to maintain comparable spot sizes. Consequently, the architecture prioritizes laser solutions with low inherent divergence and high spatial mode quality.

The distribution of receivers on the Moon is closely linked to the progress of lunar missions, ISRU missions, and human presence. In this work, we focus on a receiver located at the lunar south pole, as an example. A strength of the architecture in question is its applicability to any location on the surface, with a limited number of orbits.

2.5. Received power and power density at the lunar surface

The received optical power is determined by the transmitted optical power and by the fraction intercepted by the receiver within the ground footprint. The receiver converts the intercepted optical power into electrical power via Photonic Power Converters (PPCs). For receiver materials and wavelengths relevant to this study (e.g., around 1064 [nm]), conversion efficiencies in the range of 35%–40% are considered representative at system level, while dedicated laboratory tests are presented later to characterize performance as a function of power density, load, and temperature.

Power density on the receiver depends on both transmitted power and spot size. The system-level sizing approach adopted takes into account the spacecraft solar array area and efficiency, as well as electrical-to-optical and optical-to-electrical conversion efficiencies. This provides the quantitative basis for the subsequent sections, which detail (i) the laser payload design and beam shaping constraints, (ii) PPC performance and thermal behavior, and (iii) orbit/pointing requirements and spacecraft attitude dynamics needed to maintain the beam within the required footprint.

3. Laser system

Traditional solar power solutions, while effective on Earth, encounter significant inefficiencies in the unique lunar environment we have described: the extreme diurnal cycle collapses efficiency when energy storage is included in the overall system efficiency; at the polar regions, the Sun remains perpetually low on the horizon, therefore the need for tall masts or tracking mechanisms which increase mass and reduce reliability; once deployed, these arrays cannot easily be relocated or reoriented where needed. To address these constraints, our study explores an innovative solution: WPT from lunar orbit using high-power fiber lasers. The use of high-power laser beams in the near-infrared allows to reach very long distances while transmitting high power through a very narrow beam. The solar energy is collected by the satellites and re-converted into focused laser beams aimed at the receivers on the Moon's surface. Fiber lasers and amplifiers have the advantages of superior beam quality, high electrical efficiency, no maintenance, high reliability, compactness and ruggedness when compared to traditional diode-pumped solid-state laser systems [18,19]. Optical fibers have been widely utilized in space applications, serving as optical sensors and in optical communication terminals, particularly in the form of fiber laser amplifiers.[20,21]. Radiation-tolerant devices are available as well as space-qualified CW versions, although with low peak power. Nevertheless, these devices are scalable to very high powers with both single- and multi-device architectures. Advancements in fiber laser technology are making such a payload feasible, starting from the development of highly efficient laser diodes (leveraged from telecommunications) and special fiber optics capable of withstanding the rigors of space. Size, weight and power requirements are strong drivers in the design of a space-based instrument. Ytterbium-doped fiber lasers are currently the best-performing devices in terms of overall efficiency, including fiber and pump-diode technology. Higher electrical efficiency allows fewer pump diodes to be required, reducing the necessary weight. Despite the numerous advantages, there are still issues to be resolved when power scaling to high-power narrow-bandwidth transmission, namely nonlinear effects and thermal effects [22].

3.1. Power requirements

Early Lunar surface power users are expected to mainly be of three kinds: ISRU Lunar Habitats, and Science and Exploration users. ISRU is the largest power user requiring power levels in the order of $60 - 100$ [kW], to be used over long distances of several kilometers to mine and transport the moon's natural resources. Lunar habitats require power levels in the order of $20 - 50$ [kW] (assuming a four-member crew in the early lunar outposts) while drones and rovers exploring the lunar surface only require up to ~ 500 [W] of power [23]. It is more probable that a power beaming system complements other power generation and distribution systems, rather than working as a standalone system. The power it can transmit to the lunar surface depends on the efficiency of the various stages of conversion, from the solar power captured by the satellites to the receiver's cells. High-level efficiency contributions for the system can be considered as follows: First, we assume that the energy has already been converted and stored from the satellite's solar panels into onboard batteries, with an efficiency of approximately 30% for state-of-the-art solar cells. Next, the electro-optical efficiency of the laser system is about 40%, particularly for modern ytterbium-doped fiber lasers, which operate with 50% efficiency from laser diodes and 80% optical-optical efficiency in the Yb-doped active fiber. Finally, the opto-electric conversion efficiency of the cells in the lunar surface receiver can range between 35% and 40%, assuming the receiver captures all the incoming radiation, as described in Section 8. Overall, these components amount to about 165 [W/m^2], or 165 [W] per unit area of the spacecraft's solar arrays.

For the reference mission scenario, the electrical power system is based on the combined use of solar arrays and onboard battery storage. In particular, the solar arrays provide the primary energy generation capability, while the batteries are used to store energy outside the transmission phase and support high-power laser operation during power-beaming intervals. Therefore, the adopted power architecture is not based on direct instantaneous solar powering alone, but on a hybrid generation-and-storage approach consistent with the operational concept discussed in this work.

The full end-to-end efficiency chain adopted for the reference mission scenario is summarized in Table 2. This table clarifies the main energy conversion stages from solar collection on the spacecraft to electrical power conversion at the lunar receiver. In addition, a spacecraft-level power availability metric is reported to relate the onboard electrical power budget to the reference solar-array sizing. In this context, the quantity of 165 W/m^2 does not represent the electrical power delivered on the lunar surface, but rather the electrical power available on the spacecraft per unit solar-array area, used as a first-order sizing metric for the onboard power architecture.

As a representative reference case, the minimum energy delivered to a lunar user was determined to be 5 [kWh] for the first un-crewed surface habitat, rovers and lunar science [24]. Considering the reference efficiency chain and an approximately 20-minute power transmission window, a continuous laser power of at least 30 [kW] is needed. This value is consistent with the order of magnitude obtained in earlier architecture studies for a single transmitting satellite in a 600 [km] lunar orbit [14].

3.2. Spot diameter on the lunar surface

Although transmission happens in the vacuum of space, where the laser beams do not experience deflection or degradation due to refraction or reflection phenomena, one has to still account for diffraction. Diffraction is the result of the wave properties of light, causing the change of the beam's intensity distribution with distance. From the paraxial approximation, we also derive the expression for *Fraunhofer*

Table 2
Reference efficiency chain and spacecraft-level power availability for the lunar wireless power transmission architecture.

Stage	Symbol	Assumed efficiency	Note
Solar-to-electrical on spacecraft	η_{SE}	30%	State-of-the-art solar cells
Electrical-to-optical laser conversion	η_{EO}	36%	Yb-doped fiber laser
Optical-to-electrical at lunar receiver	η_{OE}	40 ± 5%	PPC at 1064 nm
End-to-end efficiency	η_{tot}	3.8–4.3%	Product of above stages
Available electrical power on spacecraft per unit solar-array area	$P_{\mathrm{el,sc}}/A_{SA}$	~165 [W/m^2]	Reference spacecraft-level power availability

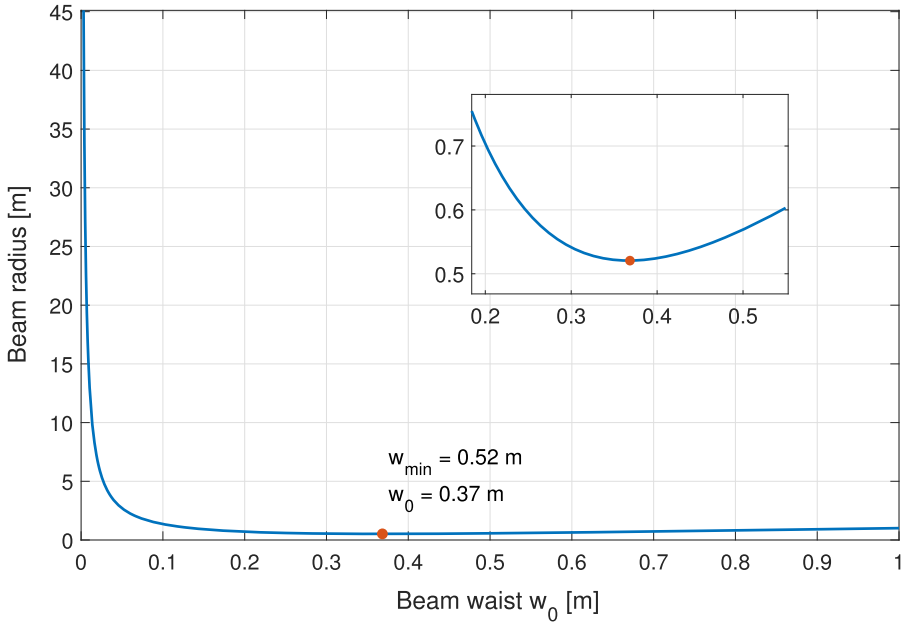


Fig. 2. Beam size $w(z)$ at 400 [km], as a function of beam waist w_0.

diffraction, which is only accurate for long distances [25]. The solution to the paraxial wave equation can be written as a Gaussian function times a quadratic phase factor, where

$$w(z) = w_0\sqrt{1+\frac{z^2}{z_R^2}}, \tag{1}$$

is the radius of the beam as a function of z. By interpreting this expression, we can make a first observation: the smallest beam radius is at z = 0, where $w(0) = w_0$ and it is called the *waist* of the beam. At $z = z_R$, the beam radius becomes $w(z_R) = \sqrt{2}w_0$. To study the behaviour of the waist, and especially its behaviour as a function of distance, we can use Eq. (1). We calculate at first the final radius of the beam at a distance of 400 [km], as a function of beam waist w_0. Being an ideal Gaussian beam, the values of $w(z)$ are the minimum possible considering natural divergence. The behaviour of the beam size as a function of its beam waist w_0 is shown in Fig. 2, with a zoom-in plot to show the presence of a minimum of the function at a certain combination of beam waist and minimum beam radius $w_{\min} = w(400)$. In any configuration at the same wavelength, beam quality and distance, there is one size of beam waist that results in the minimum beam radius at that distance. This information gives useful information for sizing the beam expanding and collimating optics. In Fig. 3, this behavior is plotted while varying the distance z. From this plot, we understand that with a beam waist of a few tens of centimeters, the size of the receiver on the lunar surface can be kept well within the 10-meter diameter limit. In fact, this limit is reached at $z > 1000$ [km], for an initial diameter of less than 10 [cm], which is a relatively small mirror to install on the satellite. As this calculation was performed considering an ideal Gaussian beam, it is then further generalized by plotting this 10-meter limit for beam qualities, in terms of the M^2 parameter. This result is shown in Fig. 4, which shows how much the quality of the beam has an influence on the distance that can be reached while maintaining the beam spot within a reasonable diameter. State-of-the-art high-power fiber lasers with output powers up to 20 [kW] (from IPG Photonics [26]) have a BPP (Beam Parameter Product) of 4. BPP is the product of the laser beam's divergence half-angle and the radius of the beam waist. The BPP and M^2 parameters are two ways of quantifying the quality of the laser beam, and how well they can be focused to a small spot or collimated for very large distances. A Gaussian beam has the lowest BPP physically possible, equal to $BPP = \lambda/\pi$ [mm mrad], where λ is the laser's wavelength. The ratio of the BPP of the real beam to that of the ideal Gaussian beam is the M^2 parameter, which becomes independent from the laser's wavelength. Assuming paraxial approximation: $BPP = \psi w_0 = M^2\frac{\lambda}{\pi}$. Therefore, the laser mentioned above has a $M^2 = 11.8$. This already limits the distances that are reachable within the limit of a 10-meter receiver and requires larger mirrors to accommodate the larger beam waist necessary. A design requirement is to use laser systems with low inherent beam divergence to maintain a narrow beam over long distances, by using single-mode fiber lasers that produce a high-quality beam with minimal divergence.

3.3. Materials and design considerations

Requesting small quantities of specialized components increases costs compared to using products typically sold in bulk. However, it could be possible that a few small changes to these products can already greatly affect the space flight readiness of the component. Identification of materials is the first step in this process, for which all materials making up the component must be known and qualified for flight. If all

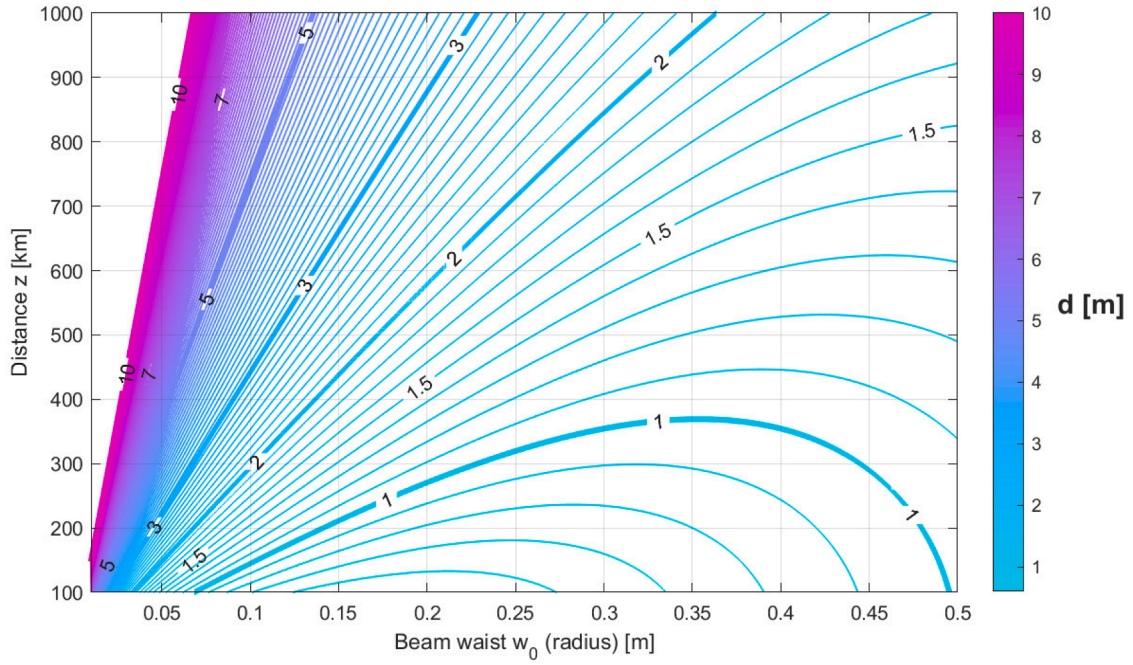


Fig. 3. Contour plot of the beam's diameter [m] as a function of distance z [km] and of beam waist w_0 [m]. Assumption of an ideal Gaussian beam is made.

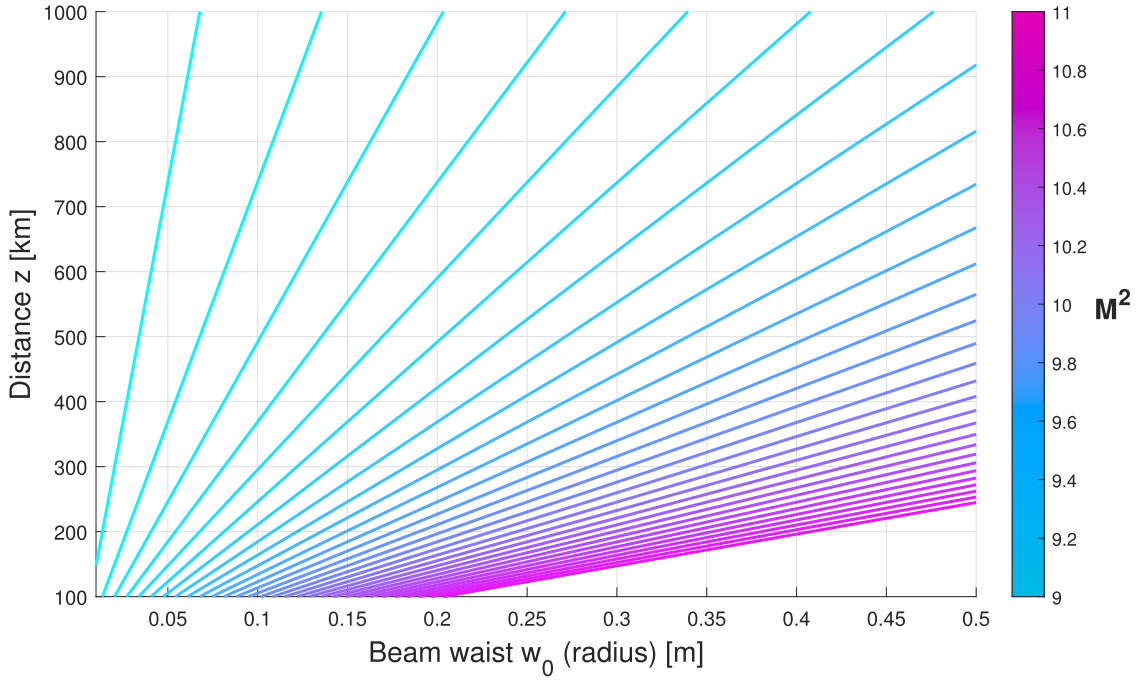


Fig. 4. 10-meter beam diameter as a function of distance z, beam waist w_0, and M^2 parameter.

component materials are not known, a destructive physical analysis can provide their identification. All non-metallic materials should be characterized for outgassing properties in vacuum. This is especially critical for a high power laser system including optical components such as mirrors and other bulk optics, in which contamination from stray material can have catastrophic effects [27]. Regarding thermal considerations, it is crucial first of all to understand the limitations of each component and its performance specification. Many commercial parts are limited to the basic standard of −25°C to +85°C, while others can be qualified for −40°C to +85°C operational temperatures. Based on the selected orbit, spacecraft attitude with respect to the Sun, operational concept, and internal subsystem accommodation, a dedicated Thermal Control System (TCS) will be designed to ensure that all components operate within their qualified temperature limits, including an additional design margin of 10°C with respect to the expected worst-case environmental conditions. Outside the Earth's magnetosphere, the space radiation primary sources are galactic cosmic rays (GCRs), solar protons and solar particle events (SPEs), [28,29], while contributions from the trapped proton and electron belts are zero. Two missions have measured the dose values at various altitudes in Lunar orbit. The Radiation Monitor (RADOM) payload onboard the Chandrayaan-1 mission performed measurements throughout its one-year mission to characterize this environ-

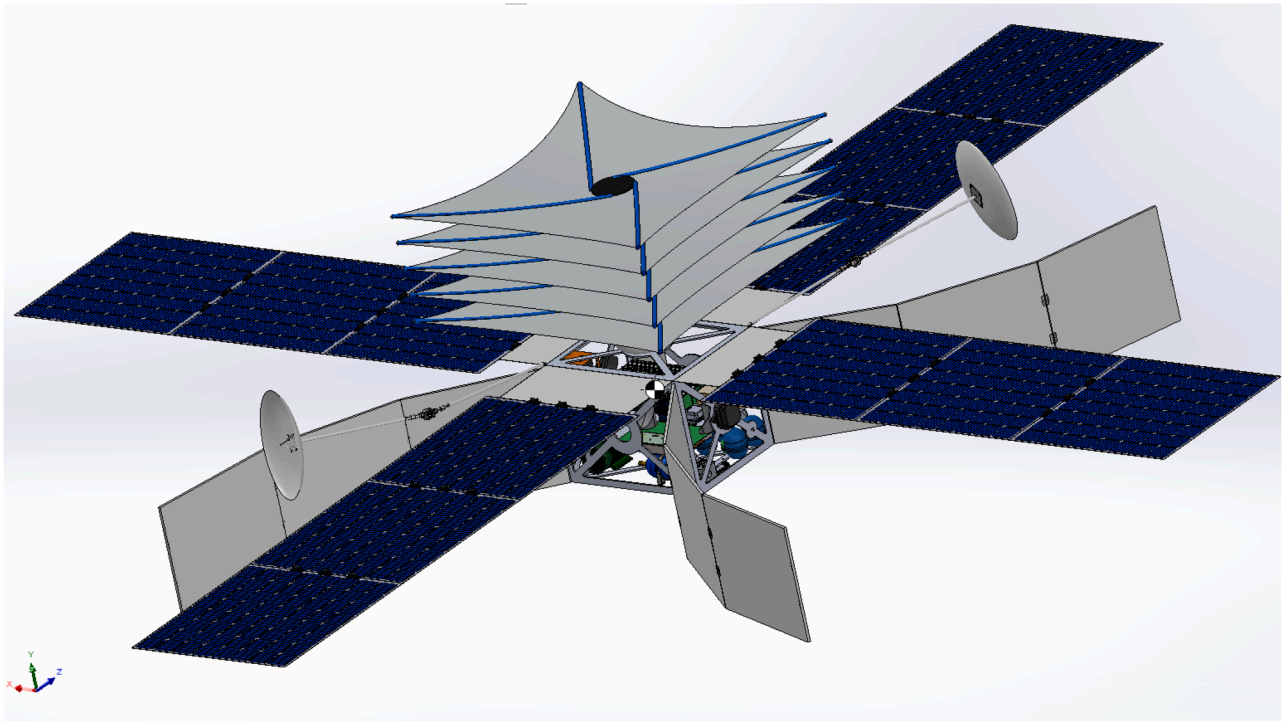


Fig. 5. External view of the satellite.

ment. The instrument revealed very small values for both particle flux [particles/cm^2/s] and radiation dose [μGy] during Earth-Moon transfer and in lunar orbits of 100 [km] and 200 [km]. The total accumulated dose during the transfer from Earth to the Moon was found to be ~ 1.3 [Gy]. Average flux and dose in lunar orbit further decreased slightly, with the lowest values found at the lowest altitudes, due to the shielding effects of the Moon. Since the solar activity minimum occured shortly after the mission ended in 2009, it is unlikely that radiation exposure will exceed the 0.257 [mGy/d] in these orbits [30]. The Lunar Reconnaissance Orbiter (LRO) mission's Cosmic Ray Telescope for the Effects of Radiation (CRaTER) instrument was also designed to characterize the global lunar radiation environment, and also measured doses values between $0.22 - 0.27$ [mGy/d] from its orbit at 50 [km] from the lunar surface. For higher-altitude orbits as the ones described in this project, the values of flux and dose would be the same as open space at Moon-distance from the Earth, minus a smaller effect of body occlusion from the Moon.

4. Inertia analysis of the satellite

Based on the requirements described above and subsequent orbital and pointing analyses, the preliminary design of the satellite was carried out. In Table 3 is presented the analyzed satellite's components and their respective masses. This analysis is essential to determine both the inertia matrix and the center of mass of the satellite, which will be used in subsequent sections to calculate the torques generated by solar radiation pressure and the lunar gravity gradient disturbances. While the Electrical Power System (EPS) has been dimensioned based on specific requirements [14], the remaining subsystems are based on initial assumptions made during the preliminary design phase. Following the selection of the components, the total weight of the system is 600 [kg]. The inertia matrix [kg m^2] relative to the system's center of mass is as follows:

$$\mathbf{I} = \begin{bmatrix} 957.56 & 1.95 & -5.85 \\ 1.95 & 1834.18 & 2.16 \\ -5.85 & 2.16 & 980.92 \end{bmatrix} \tag{2}$$

Table 3
Mass breakdown of satellite components.

Component	#	Weight [kg]
Honeywell HC9 RWs	4	22
Gyroscope Sensor	2	1.5
Star Trackers	2	0.5
On-Board Computer	1	1.5
Comm Antennas	7	6.5
Electric Power System	1	139
Solar Panels (21 m^2)	4	160
Laser Box	1	45
Thruster	7	12
Tanks	6	6
Structures	1	80
Inflatable Structure (Sunshield)	1	6
Thermal System Pump	1	30
Accumulator	1	20
Cold Plate	1	20
Radiator Panels	4	45
Sunshield	1	5
Total Weight		**600**

Fig. 5 presents the 3D model of the satellite, illustrating its body axes and center of mass.

5. Orbital requirements

Several studies have been conducted analyzing lunar communication and transmission mission scenarios and associated requirements [31–35]. Most studies are focused to obtain orbital architectures such that global coverage of the Moon can be achieved, in anticipation of a future where missions will be conducted over the entire lunar surface. In particular, in [36] it is analyzed, through an analytical hierarchy process, which is the best mission scenario trade-off for energetically supplying the vicinity of Shackleton crater since it is the first construction site for lunar bases chosen. The optimal option is chosen through a systematic series of objective pairwise comparisons between some figure of merits, allowing for the determination of attribute weightings

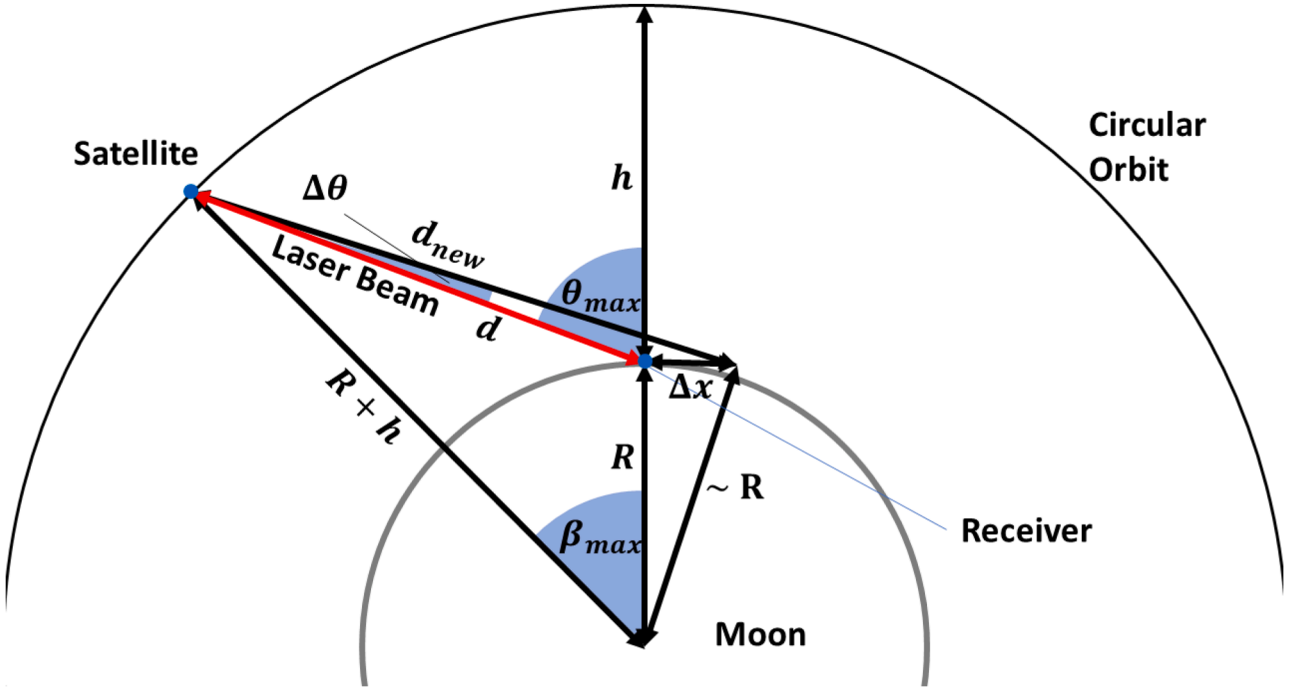


Fig. 6. Schematic diagram of the architecture consisting of satellite, Moon, receiver and transmission cone.

as well as scoring alternatives. These figure of merits include the number of satellites, mission simplicity, spacecraft mass, stability of the orbit, mission cost and mission feasibility. Moreover, the orbital architectures considered included 2BP LLO (Low Lunar Orbits) and CR3BP High Near Circular Lunar Orbits with respectively altitude between [0 – 100] and [9000 – 11000] [km], and CR3BP L2 Southern Near Rectilinear Halo Orbit (NRHO), CR3BP Quasi-Frozen Orbits and finally CR3BP Butterfly Orbits with radius at periapsis respectively between [1800 – 4000], [200 – 600] and [1800 – 4000] [km]. In particular, CR3BP Quasi-Frozen Orbits have the highest score [36] and reflects best the characteristics of a lunar transmission mission scenario. These orbits exploits the non-uniform gravitational potential of the Moon and the Earth's third body influence to maintain quasi constant the required orbital parameters for a more efficient transmission, i.e. semimajor axis, eccentricity and inclination. In this sense, for a matter of simplification for deriving the accuracy and angular velocity requirements of pointing systems, as a first approximation, we consider orbits with fixed orbital parameters, i.e. considering the 2BP orbital model.

5.1. Pointing accuracy

For circular orbits, the tangential velocity of an orbiting object is

$$v_\theta = \sqrt{\frac{\mu_{\mathbb{C}}}{R_{\mathbb{C}} + h}} \quad , \tag{3}$$

where $\mu_{\mathbb{C}}$ is the gravitational constant of the Moon (4.9×10^3 [km^3/s^2]), while $R_{\mathbb{C}}$ is the radius of the Moon and h is the height of the circular orbit. The architecture of the WPT system is shown in Fig. 6 where $\theta_{\max}$ is the maximum angle relative to what is called the transmission cone. Transmission cone means the geometric cone, in this case for simplicity in the 2D plane, composed of the vector drawn when power transmission by the laser beam begins, between the satellite and the receiver, and the same vector drawn when transmission stops. $\theta_{\max}$ is a parameter on which pointing requirements depend, as large thetas imply greater energy transmission and thus greater energy stored by the cells, but at the same time the required precision of pointing. From simple geometric considerations, the angle $\beta_{\max}$, formed by the vector connecting the satellite at the beginning of the trasmission and the center of the Moon, and the vector connecting the center of the Moon to the center of the transmission cone can be calculated as

$$\beta_{\max} = \theta_{\max} - \arcsin\left(\frac{R_{\mathbb{C}}}{R_{\mathbb{C}} + h}\sin(\theta_{\max})\right) \quad . \tag{4}$$

The total time the satellite in circular orbit spends in the transmission cone is

$$t_c = \frac{2\theta_{\max} - 2\arcsin\left(\frac{R_{\mathbb{C}}}{R_{\mathbb{C}}+h}\sin(\theta_{\max})\right)}{\omega} \quad , \tag{5}$$

where ω is the angular velocity of the satellite in circular orbit, computed as $\sqrt{\mu_{\mathbb{C}}/(R_{\mathbb{C}} + h)^3}$. The β angle, positive in the clockwise direction is calculated as $\beta = -\beta_{\max} + \omega t$. The vector simulating the laser beam is geometrically represented as

$$d = \sqrt{(R_{\mathbb{C}} + h)^2 + R_{\mathbb{C}}^2 - 2(R_{\mathbb{C}} + h)R\cos(\beta)}. \tag{6}$$

The angle θ formed with the perpendicular vector is:

$$\theta = \frac{\arcsin(h + R_{\mathbb{C}})}{d}\sin(\beta) \tag{7}$$

Assuming that the maximum linear error we want to make on the receiver is $\Delta x = 1$ [m] and that the lunar surface relative to the receiver dimension can be considered linear, we have $\Delta\beta = \arcsin(\Delta x/R_{\mathbb{C}})$. From here, the new beta can be calculated by adding the old beta to the delta, and consequently, the new distance d. This geometry is visible in Fig. 6. Therefore:

$$\Delta\theta = \arctan\left(\left(\frac{d}{\Delta x\cos(\theta)} + \tan(\theta)\right)^{-1}\right) \tag{8}$$

The $\Delta\theta$ thus represents the error angle, known as the pointing error, allowed so that linearly, on the target placed on the lunar surface, an error of 1 [m] is made. Considering, for example, a circular orbit at 600 [km], the allowed angular errors are in the order of [μ rad]. FSMs (Fast Steering Mirrors) are available in various types, each designed for specific purposes: Mechanical, Piezoelectric (PZT) and Micro-Electromechanical (MEMS). PZT FSMs are known for their outstanding precision and quick response times, but they are limited by a small angular motion range.

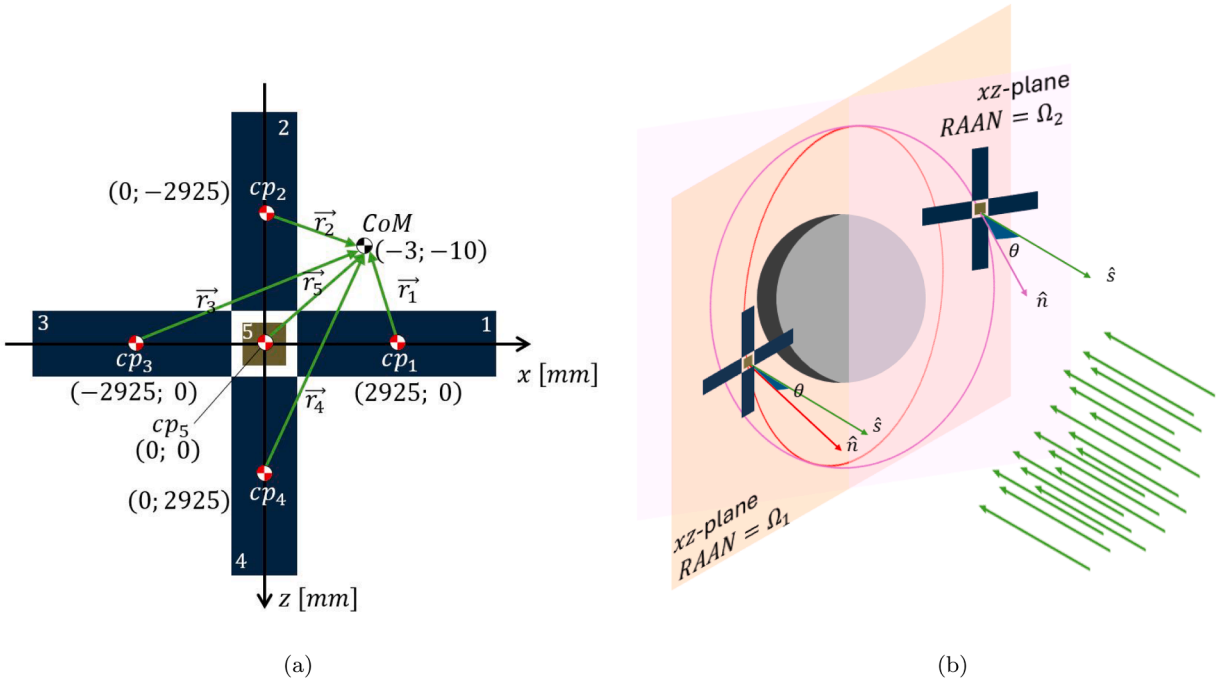


Fig. 7. **a** Schematic representation of the satellite's surfaces. **b** Variation of the angle θ as a function of the RAAN.

Moreover, their operation often demands sophisticated closed-loop control mechanisms. In this particular application, the extremely high precision required necessitates piezoelectric actuators, bringing in the challenge of limited tilt range. Efficient heat dissipation from these mirrors is achieved using specialized heat management systems. A second mechanical stage is introduced to extend the tilting range, employing systems like gimbals or more advanced hexapods. This is essential since current FSM technology typically only achieves tilt ranges in the microradian range. Achieving accurate mirror positioning depends on initial calibration, and technologies like gimbal and hexapod systems are being considered. Hexapods, with their six degrees of freedom, offer superior accuracy and are already used in satellites for precise pointing applications, such as sensors and cameras. Another very important issue, not directly addressed in this paper but currently being worked on for the final architecture of the wireless power transmission system, is how to recognize the target and track it during transmission while the satellite follows its orbital movement. In the proposed system, the receiver location on the lunar surface is known a priori by mission design, as it is pre-deployed and accurately georeferenced. Target tracking during the orbital pass is therefore driven by onboard navigation rather than target acquisition. The spacecraft estimates in real time its orbital state using optical navigation techniques, such as horizon-based Optical Navigation, providing position accuracy on the order of tens to hundreds of meters in low lunar orbit. If required, this performance can be further improved through sensor fusion with a radio link between the spacecraft and the surface receiver, enabling one-way or two-way ranging to reduce the navigation uncertainty.

6. Estimation of external disturbance torques

In this section, we will examine the two main external factors that influence the satellite's attitude: the lunar gravity gradient and the solar radiation pressure. For this initial analysis, we also disregard the effects of albedo pressure, thermal radiation, and Moon's non-uniform gravitational potential, given the Moon's low albedo, average temperature and the short simulation time (almost 19 minutes). Solar radiation pressure is caused by the interaction of solar photons with the satellite's surfaces. The pressure is proportional to the solar radiation intensity, I_s approximately 1361 [W/m^2] at Earth's average distance from the Sun, i.e 1 AU= 1.49597870×10^8 [km]. The total force exerted by solar radiation, $\mathbf{F}_{s,tot}$, on a satellite is thus the vector sum of the forces exerted on each surface:

$$\mathbf{F}_{s,tot} = \sum_i \frac{I_s}{c} A_i \cos(\theta_i)(1+\rho_i)\mathbf{n}_i \tag{9}$$

where c is the speed of light in a vacuum, approximately 3×10^8 [m/s], A_i is the area of the ith surface, θ_i is the angle of incidence of the radiation with respect to the normal to the ith surface, ρ_i is the reflectivity coefficient of the ith surface and $\mathbf{n}_i$ is the unit vector normal to the ith surface. For this analysis, we consider the worst-case scenario: the xz-plane is assumed to be the most exposed to the Sun; Figs. 7a, b and 8 illustrate the case study graphically.

The solar panels are located in this plane, and since they represent the largest surface area, the resulting force from solar radiation pressure will be the highest. As shown in Fig. 7a, the satellite is modeled as having five primary surfaces: four solar panels of equal size, each with an area of 1.32×3.96 [m], and one face with an area of 0.85×0.85 [m], covered with Kapton coated with aluminum to enhance shielding from solar radiation. The reflectivity coefficient ρ is assumed to be 0.1 for the solar panels, while for the Kapton/aluminum surface, it is 0.7. Solar radiation exerts a moment, $\mathbf{M}_s$, relative to the satellite's center of mass, which is calculated as:

$$\mathbf{M}_s = \sum_i \mathbf{r}_i \times \mathbf{F}_{s,i} \tag{10}$$

where $\mathbf{r}_i$ is the position vector of the center of pressure of the ith surface relative to the satellite's center of mass, and $\mathbf{F}_{s,i}$ is the force acting on the ith surface. To compute the angle θ in Eq. (9), it is necessary to define the satellite's orbital parameters. Given the short simulation period (18 minutes and 43 seconds), corresponding to the satellite's transmitting time, its position is calculated using the two-body problem, starting from the orbital values: the semi-major axis is 4337.4 [km], the eccentricity is 1×10^{-15}, the inclination is 89 [°], and the argument of perigee is 90 [°]. The Right Ascension of the Ascending Node (RAAN) is yet to be defined. The mean anomaly is 0 [°], and it is computed at the reference time of January 1, 2000, 12:00 TDB. The angle θ_i is computed as the angle between the satellite-Sun unit vector, $\hat{s}$, and the unit vector, $\hat{n}$,

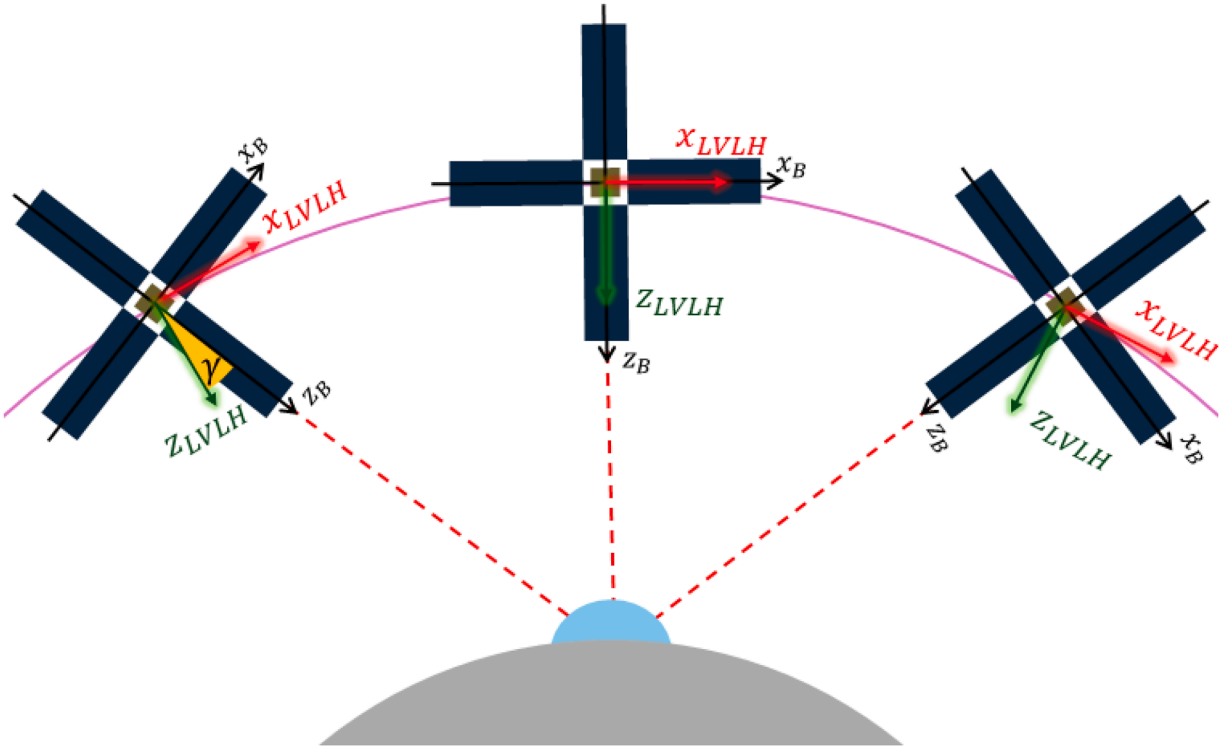


Fig. 8. Configuration of the coordinate axes for computing the solar disturbance moment $\mathbf{M}_s$.

normal to the ith surface. The unit vector $\hat{s}$, as a function of time, was determined using lunar ephemerides obtained from the Horizon System of the Jet Propulsion Laboratory, combined with the satellite's position. The computation parameters were set as follows: Start date = 2030-01-01 12:00 TDB, End date = 2030-01-01 14:49, with a time step of 1 minute and a reference frame centered on the Sun. To simulate the worst-case scenario, $\cos(\theta)$ must be maximized, implying small angles between $\hat{s}$ and $\hat{n}$. As illustrated in Fig. 7b, depending on the orbital plane, the values of θ can vary significantly with changes in the RAAN. The minimum θ occurring at $\Omega = 10.80$ [°], corresponding to January 1, at 12:00 TDB.

The time evolution of θ for the selected RAAN was analyzed, showing a minimal variation throughout the entire orbit. Specifically, the minimum value of θ measured is 0.9936[°], while the maximum value is 0.9962[°]. This small variation implies that the torque $\mathbf{M}_s$ generated by the solar disturbance can be considered essentially constant. The torques around the x and z axes, $M_{s,x}$ and $M_{s,z}$, exhibit negligible variation, with values on the order of 10^{-13} [Nm]. In particular, $M_{s,x}$ is approximately -1.0997×10^{-6} [Nm], while $M_{s,z}$ is around 3.2992×10^{-7} [Nm]. The torque around the y axis, $M_{s,y}$, remains zero due to symmetry considerations. In this study, it is assumed that the xz-plane remains consistently aligned with the orbital plane, and that the z-axis always points towards the receiver. As a result, the torque around the y-axis is effectively null.The satellite's center of mass is nearly aligned with the geometric center of the pressure centers of the five main surfaces, which significantly minimizes torques from solar pressure disturbances. However, any substantial misalignment could increase the torque, complicating the design of the attitude control system. Then, the gravity gradient torque, the other key disturbance denoted as $\mathbf{M}_{gg}^b$, measured in the spacecraft body frame, can be expressed as [37]

$$\mathbf{M}_{gg}^b \approx \frac{3\mu}{||\mathbf{r}||^3}\mathbf{c} \times \mathbf{I}\mathbf{c} \tag{11}$$

where μ is the gravitational parameter of the central body, $\mathbf{r}$ is the position vector relative to the central body measured in the spacecraft body frame, $\mathbf{I}$ is the body inertia tensor about the satellite's center of mass while the vector $\mathbf{c}$, that contains the direction cosines of the local vertical direction as observed in the body reference frame, is computed as $\mathbf{c} = \mathbf{A}\frac{\mathbf{r}}{||\mathbf{r}||}$, where $\mathbf{A}$ is the Direction Cosine Matrix. In Fig. 9, the torques induced by the lunar gravity gradient on the satellite's body axes over time are illustrated. The torques are shown only during the period when the satellite is transmitting power to the receiver, specifically 75 minutes after 12:00 TBD on January 1, 2030, and for a duration of 18 minutes and 43 seconds.

Additionally, the disturbances induced by the Earth's gravity gradient were also calculated; however, since these are on the order of 10^{-13} [Nm], they have been neglected. The simplifications in this study serve as preliminary inputs to estimate key parameters and assess the control system's performance under simplified conditions. As the satellite's mass distribution and geometry are further refined, the model will be adjusted to account for additional complexities, enabling more accurate predictions and the development of a more robust attitude control system for a wider range of scenarios.

7. Attitude control system design

Starting with the inertia matrix and weight, estimated using the CAD presented earlier, an analysis was made of the attitude control system of this satellite, focusing on the use of Reaction Wheels. The purpose of attitude control, during the firing phase, i.e. within the cone of visibility, is to rotate around an axis, in this case the y-axis, by the angle relative to the cone of visibility, as can be seen in Fig. 8, in the calculated orbital time. This allows the aiming system to start its control from a system already oriented towards the target, with precision depending on the attitude control itself. The attitude control system of the satellite was simulated using Matlab&Simulink. The control to calculate the control moments to be supplied to the reaction wheels is a quaternion feedback control [38]

$$\mathbf{K}_p = [\alpha\mathbf{I} + \beta\mathbf{1}]^{-1} \tag{12}$$

$$\mathbf{K}_d = diag(d_1, d_2, d_3) \tag{13}$$

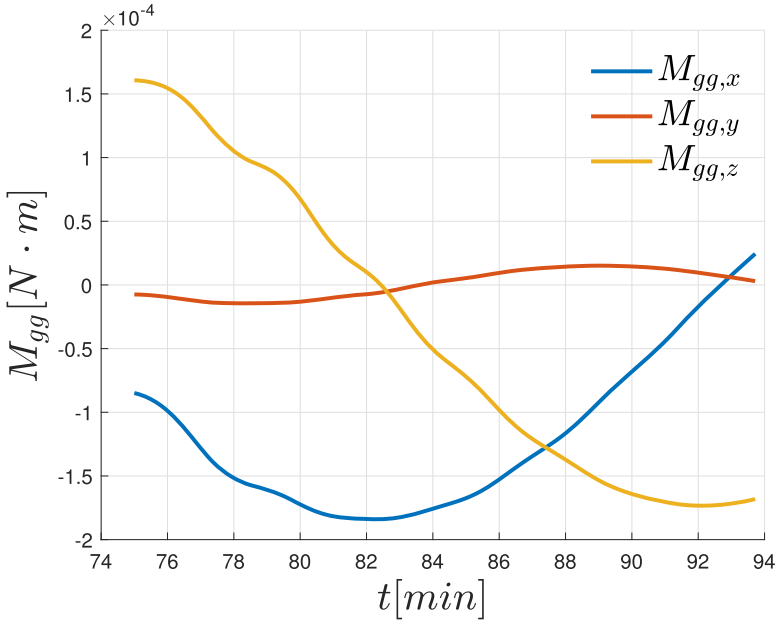


Fig. 9. M_{gg} induced by the lunar gravity vs time.

where d_i are positive scala costants, $\mathbf{1}$ is the 3×3 identity matrix, $\mathbf{I}$ is the 3×3 inertia matrix and α and β are non-negative scalars. The moment vector is thus calculated as

$$\mathbf{M}_C = -\mathbf{K}_p \mathbf{q}_e - \mathbf{K}_d \boldsymbol{\omega}_b. \tag{14}$$

The Euler equations is

$$\dot{\boldsymbol{\omega}}_B = \boldsymbol{I}^{-1}(\boldsymbol{M}_{ext} - \boldsymbol{M}_{RW} - \boldsymbol{\omega}_B \times (\boldsymbol{I}\boldsymbol{\omega}_B + \boldsymbol{h}_{RW})), \tag{15}$$

in our case the external moment is characterised by disturbances. The Reaction Wheels are schematised with a low pass filter and a saturation function and they are arranged in a pyramid configuration. Mathematically, to transform the control moment, calculated in body axes, in the 4 directions in which the RWs are arranged, a Z matrix is used

$$\begin{bmatrix} c(\beta)c(\alpha) & -c(\beta)s(\alpha) & c(\beta)c(\alpha) & c(\beta)s(\alpha) \\ c(\beta)s(\alpha) & s(\beta)c(\alpha) & -c(\beta)s(\alpha) & -c(\beta)c(\alpha) \\ s(\alpha) & s(\beta) & s(\beta) & s(\beta) \end{bmatrix}$$

In this matrix, α in our case is equal to 0 while β, as can be seen in [39], is 30°.

$$\boldsymbol{M}_{4RW} = \boldsymbol{Z}^{-1}\boldsymbol{M}_C \tag{16}$$

where $\boldsymbol{Z}^{-1}$ means the pseudo-inverse matrix of Z and $\boldsymbol{M}_{4RW} \in \boldsymbol{M}^{4x1}$. At this point, it is possible to calculate the moment along the axy bodies

$$\boldsymbol{M}_a = \boldsymbol{Z}\boldsymbol{M}_{4RW} \tag{17}$$

In this study, a circular lunar orbit at 600 [km] was chosen for simplicity. Assuming a transmission cone angle of 60[°] ($\theta_{\max}$ shown in Fig. 6), the laser transmission total angle will be 120[°], in a time of approximately 1123 seconds, as explained in Eq. (5) . Since translational and attitude motion are de-coupled, we take as initial and final quaternions those shown in Table 4. The initial quaternion represents a body reference system, rotated around y_{LVLH} by 40.07[°] with respect to the LVLH reference system, at the moment the satellite enters the transmission cone. This angle is represented in Fig. 8 as γ. This body reference system during the simulation is rotated by exactly 120[°] (2 times $\theta_{\max}$) around the y body axis. The satellite's rotation system must also be able to counteract the disturbances, including those due to solar pressure and gravity gradient. Figs. 10–12 and are shown the results for the quaternions mentioned above, the moments to be applied for each RWs and the final rotation of the z-axis body with respect to itself at the beginning of the transmission. It can be seen that the satellite's rotation system works correctly and therefore the satellite will follow, within the transmission cone, the receiver placed on the surface, with the pointing system being able to isolate from micro-vibrations and complete the pointing of the laser starting from a satellite already correctly rotated. The presented attitude control ensures that the residual pointing error falls within the capture range of the Fine Steering Mirror subsystem, which is responsible for sub-arcsecond beam stabilization.

Table 4
Control parameters and initial conditions.

Variable	Symbol	Value
Satellite Mass	m_c	600 [kg]
Max Torque RWs	$T_{\max}$	0.2 [Nm]
Initial Quaternion	q_0	[0.939, 0, 0.342, 0]
Final Quaternion	q_d	[0.174, 0, 0.984, 0]
Filter Time Constant	τ_{RW}	0.01 [s]
Control Gain α	α	0.0001
Control Gain β	β	0.01
Boundary Layer Width	d	10

8. Photonic power converter tests and validation

A Photonic Power Converter (PPC) is a phototransducer that converts narrow-band photonic energy into electricity. It is essential in optical power transmission systems, which deliver power as light through free space or optical fiber. At the receiving end, the PPC converts photonic energy to electricity to power electronic components. The most efficient PPC to date is a five-segment PPC with a vertical stack structure, achieving a power conversion efficiency of 70% [40]. This efficiency is due to the use of Gallium Arsenide (GaAs), known for its excellent performance at wavelengths of 810 – 850 [nm] [41,42]. Although GaAs is effective for certain wavelengths, optimizing system efficiency involves other materials. The efficiency of an optical power transmission system depends on the PPC's efficiency, as well as source and transmission efficiencies. Optical fibers show higher transmission efficiency at longer wavelengths, which GaAs does not optimally convert. Materials such as GaAs, Indium Gallium Arsenide (InGaAs), and Indium Aluminum Gallium Arsenide (InAlGaAs) are used in PPCs based on their bandgaps matching the radiant energy of the specified wavelength. For a wavelength of

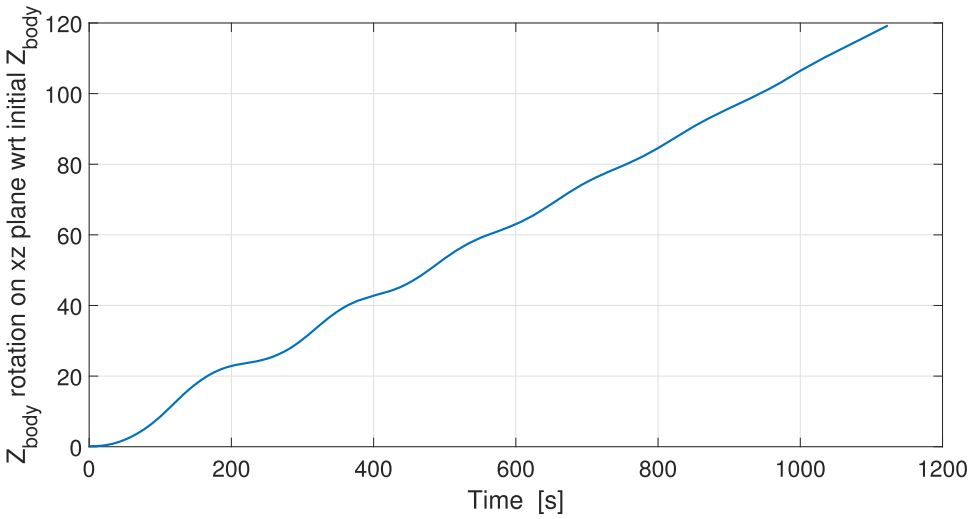


Fig. 10. Z_{body} rotation during the transmission.

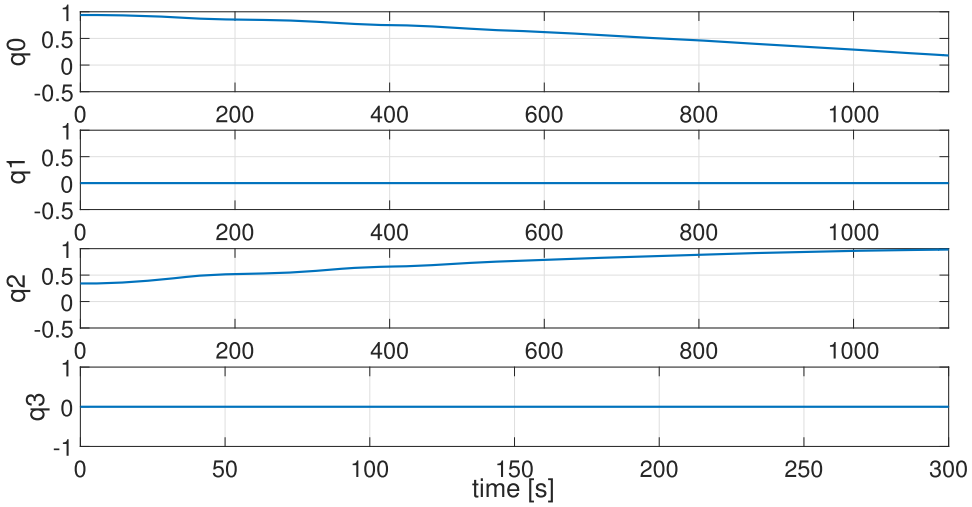


Fig. 11. Quaternions vs time in the transmission cone.

1064 [nm], suitable materials include Gallium Indium Arsenide Phosphide (GaInAsP), InGaAs, and InAlGaAs, with conversion efficiencies from 35% to 40%. In 2001, Green demonstrated that monochromatic PV conversion could theoretically reach 100% efficiency at infinite input intensity [43]. However, real-world limitations reduce this efficiency. Improving material quality, operating closer to the GaAs bandgap, and increasing light intensity can enhance PPC efficiency [44]. Each order of magnitude increase in light intensity boosts efficiency by about 4%, and redesigning for 850 [nm] can reduce thermalization losses by 2%. Combining these improvements, overall device efficiency could exceed 80%, advancing PPC technology and optical power transmission.

8.1. Tests and relevance of the experimental campaign to the system design

This section presents some tests conducted aiming to demonstrate the feasibility and efficiency of illuminating solar cells using high-power laser sources. Although the present work is primarily focused on the preliminary design of a lunar-orbital laser WPT architecture, the receiver-side Photonic Power Converter (PPC) performance is a first-order driver for system sizing and feasibility. In particular, realistic PPC efficiency and thermal behavior under high optical power density directly impact (i) the required transmitted optical power to meet a given delivered electrical power at the surface, (ii) the allowable power-density envelope at the receiver, and (iii) the thermal control provisions needed to prevent performance degradation and/or irreversible damage. For this, the experimental campaign reported in this section is used to (a) quantify the deviation from ideal/datasheet conversion performance under representative illumination conditions, (b) assess the sensitivity of conversion efficiency to electrical load and temperature rise, and (c) identify practical operating limits in terms of power density and thermal margins. These results provide technology-grounded inputs for receiver sizing and calibration, end-to-end efficiency budgeting, and subsequent subsystem qualification steps. New studies and tests on the effective cooling of these cells and on the management of payloads and storage systems on the lunar surface are already planned.

To relate the laboratory campaign to the reference mission design, it is useful to compare the optical power density tested on the PPCs with the average irradiance associated with the orbital transmission scenario adopted in this work. For the representative case of a 30[kW] optical transmission and a ground footprint constrained within a diameter of about 10[m], the average optical power density on the lunar surface is on the order of 3.8×10^2 [W/m^2], i.e., about 0.038 [W/cm^2]. This value is significantly lower than both the power densities tested in the experimental campaign, which ranged from about 4.87 [W/cm^2] up to 49.86 [W/cm^2], and other experimental results reported in literature with other cell materials for laser power conversion [45].

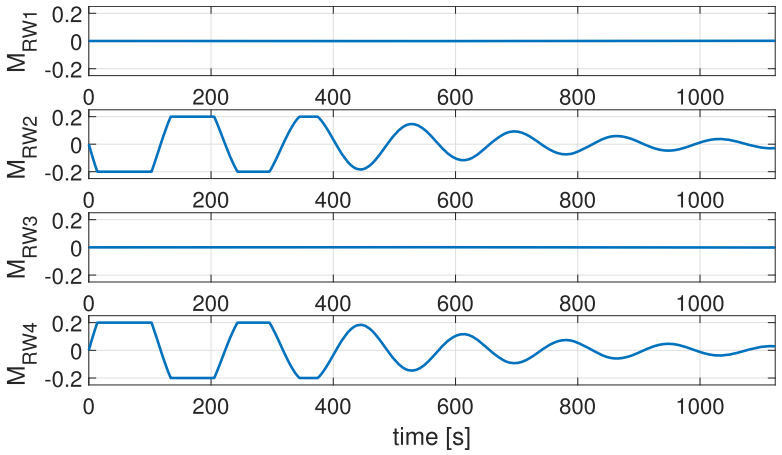


Fig. 12. RWs Torque.

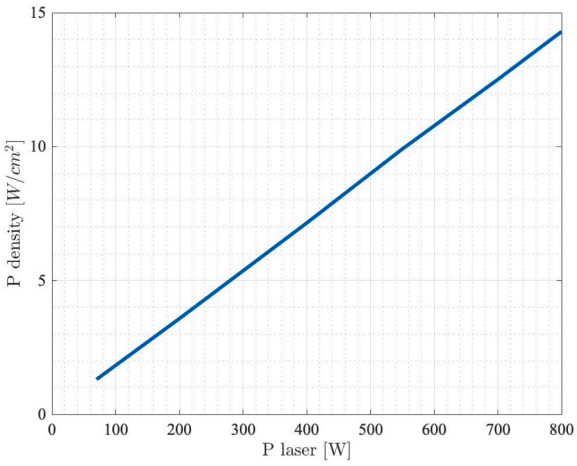
This difference is expected, since the present experiments were not intended to reproduce the full mission-scale beam footprint directly. Instead, they were designed to characterize the intrinsic PPC behavior under controlled local illumination, with particular emphasis on conversion efficiency, load dependence, thermal rise, and damage thresholds. In this sense, the tests provide upper-bound and local-operating-condition data that are highly relevant for the design of receiver submodules, for the assessment of thermal margins, and for future receiver architectures based on modular interception, optical concentration, or non-uniform flux management. Therefore, the experimental campaign should be interpreted as complementary to the mission design: the orbital analysis defines the large-scale beam delivery conditions, while the laboratory tests identify the practical PPC operating envelope and the thermal constraints that must be respected when translating the received optical flux into electrical power at receiver level.

8.1.1. Test #1: Cell illumination for WPT test

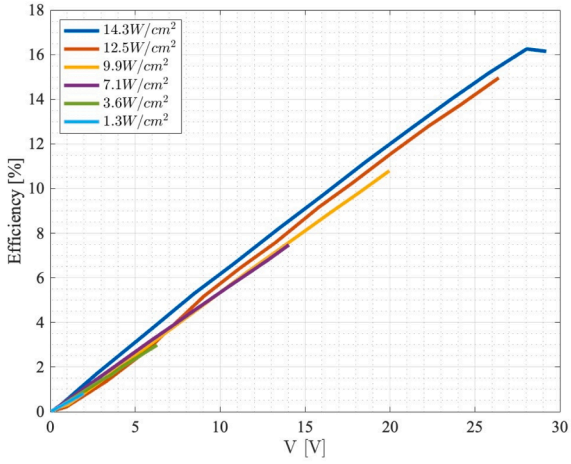
The cell employed for the tests is a MIH® VMJ PV Cell Array for 1064 [nm] laser, square of 2 [cm] side that according to datasheet has been tested up to the maximum power density value of 11.2 [W/cm^2] with a declared efficiency of 23.3%. For the illumination of the cell only one laser source was sufficient and a manipulation of the collimated beam was needed since the real gaussian beam profile of the field intensity was not perfectly suitable for the cell. To guarantee a uniform distribution of the power upon the cell's surface and to optimize the efficiency of the conversion only one of the two beams was truncated. This option certainly results in a large power loss and consequently inefficient conversion, but the goal of these initial tests is to verify the conversion efficiency of the cell alone. Referring to the gaussian beam's theory [46], in order to obtain a uniform illumination, a truncation ratio lower than 0.5 is needed. A beam expander with a subsequent aperture has been simulated: using a plano-convex lens, the collimated beam has been expanded to reach a uniform intensity distribution over the entire usable area of the cell intended as a circle of 28 [mm] diameter and then cropped through a circular aperture of the same diameter. The optimal configuration was computed to be with the aperture placed at 650 [mm] from the defocusing lens where the beam is expected to have a diameter of 112 [mm] ($1/e^2$). In this configuration, the truncation ratio results to be 0.25 with 88.25% truncated (lost) power, and a beam with constant uniform distribution over the cell area. A benchtop setup was realized for the experimental cell characterization as shown in Fig. 14. A water-cooled anodized steel plate with a 28 [mm] aperture that was designed to truncate the beam to the desired size and serve as housing for the cell. The cell's temperature was monitored using a thermal camera positioned in front of it. The thermo-chiller's water temperature was maintained at 5°C, and a threshold temperature of 120°C was set to prevent cell damage, as indicated by the datasheet. During this test session, solar cells was characterized using a rheostat as a high-power resistive load. The cell was exposed to increasing optical power levels, ranging from 70 to 800 [W], achieving a maximum power density of 14.3 [W/cm^2]. The power transmitted through the aperture was measured before placing the cell in its housing with an optical power meter. The relationship between emitted power and power density on the cell is shown in Fig. 13a. The generated current and converted power were calculated by measuring the voltage drop across a 60 [Ω] rheostat. The results of the characterization process are presented in Fig. 13b and c. The data from the experimental characterization indicates that the cell can effectively convert laser optical power into electrical power, although there are significant differences compared to the manufacturer's datasheet. The experimental results showed that conversion efficiency is highly dependent on the load value. Unlike the datasheet, which suggests the optimal load decreases with increasing power density (in the range of 10 [Ω] to 60 [Ω]), the experiments found that efficiency increases with the load, except at the highest tested power density where an optimal load of 55 [Ω] was identified. The measured efficiency values were lower than those reported in the datasheet, which ranged from 20% to 23%. The maximum efficiency achieved in the experiments was 16.3% at a load of 55 [Ω] and a power density of 14.3 [W/cm^2]. All efficiencies are based on operating only at the 1064 nm single laser wavelength for which the cells have been designed. The datasheet values are based on ideal conditions with a constant temperature of 20°C. The manufacturer notes a 3% efficiency drop for every 10°C increase in temperature. Despite the coolant being kept at a low temperature, the cell's temperature exceeded 20°C at power densities of 3.6 [W/cm^2] or higher, which may explain the lower measured efficiency at higher power densities. Maximum efficiency value and temperature measurements relative to power density are shown in Fig. 15a, b.

8.1.2. Test #2: Slightly different characterization and stress test

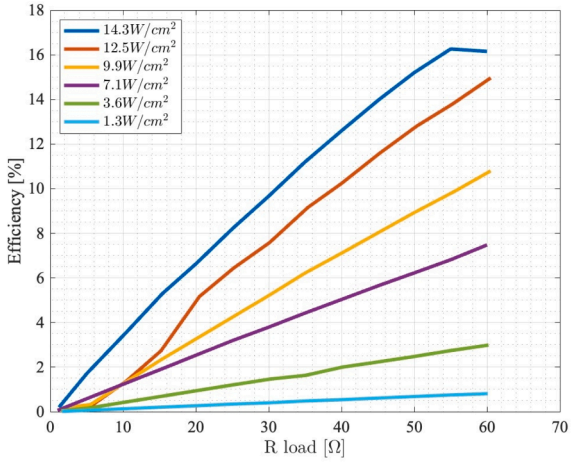
The last tests conducted aimed to assess the resistance of various photovoltaic cells when exposed to high power laser beams with a power density significantly exceeding the declared limit. The objective was to investigate how their conversion efficiency evolves under stress conditions. The employed setup is similar to the one used for the previous test. A new characterization of the cell was conducted using an updated setup, varying the rheostat resistance and maintaining an average power density of 9.97 [W/cm^2], close to the producer's maximum of 11.2 [W/cm^2]. The cell exhibited slightly lower efficiency compared to previous tests, achieving a maximum efficiency of 11.4% with a 50[Ω] load. This reduction in performance may be attributed to the different beam characteristics resulting from the new focal length, which altered the cell's operating conditions. Following these findings, a second charac-



(a)



(b)



(c)

Fig. 13. **a** Power density on the cell as a function of emitted laser power. **b** Cell efficiency versus voltage measured on the load. **c** Cell efficiency versus load resistance.

terization at an average power density of 4.87 [W/cm^2] was performed before proceeding with damage tests. Detailed efficiency results are presented in Fig. 15c. Additionally, in Fig. 15d is evident that in this case, the cell reached significantly higher temperatures, likely due to poorer heat dissipation. It is also plausible that the reduced efficiency and increased temperature are attributable to potential damage sustained by the cell during previous tests. Subsequently, damaging test started. This test involved gradually increasing the power density incident on the cell at 910 [mm] from the focal lens, using the load that had previously yielded maximum efficiency values (50[Ω]). The test was carried out in

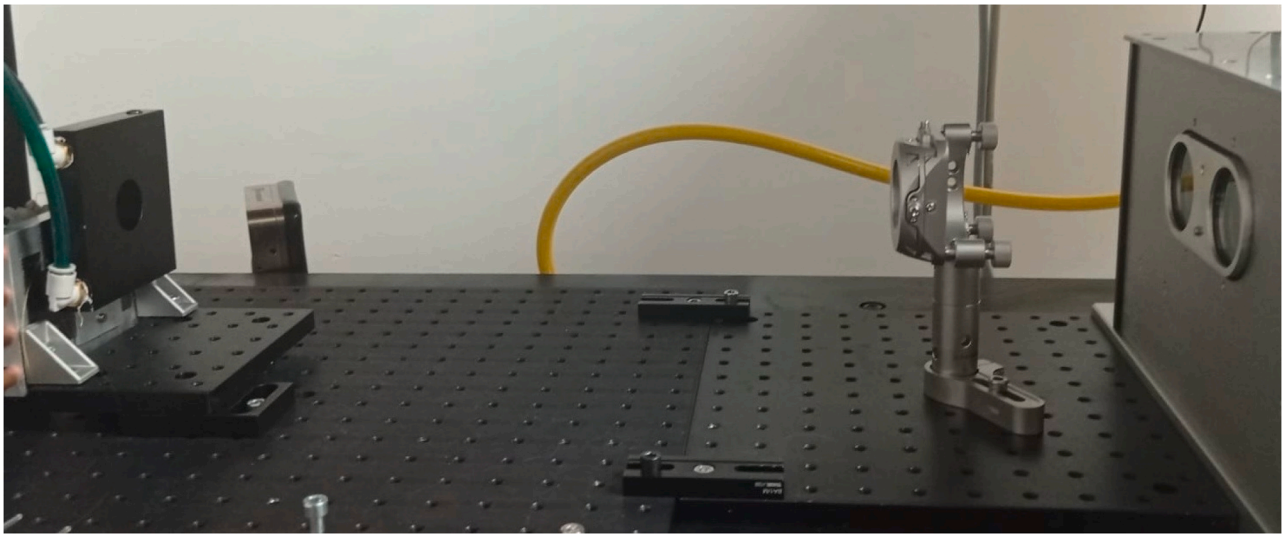


Fig. 14. Experimental setup for characterizing solar cells.

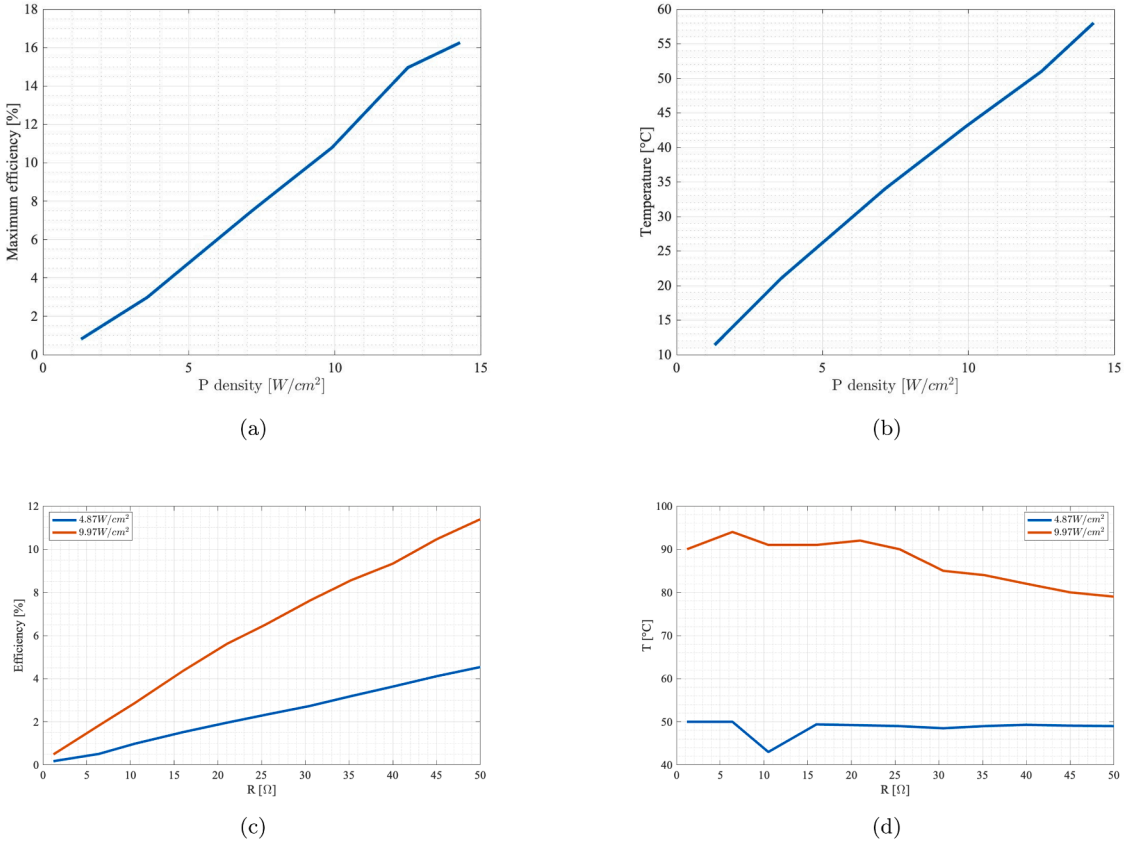


Fig. 15. **a** Maximum efficiency value obtained versus power density. **b** Temperature measurements relative to power density. **c** Conversion efficiency of the cell versus rheostat resistance. **d** Temperature trend during characterization.

a protected environment, with the entire optical path and the cell enclosed in a metal casing. In Fig. 16 is shown that inside the enclosure, a thermal camera and an auxiliary camera were used to monitor the cell during laser beam exposure. The cell sustained damage at an average power density of 49.86 [W/cm^2]. Throughout the procedure, the cell's temperature and efficiency were monitored. At the point of damage, the power output dropped to zero, and the auxiliary camera detected smoke emanating from the cell housing. Immediately after the damage, a further characterization was performed to compare results and assess the impact on the cell's performance. All collected data are presented in Fig. 17a and b, with the point of damage marked by a red vertical line. A noticeable decrease in efficiency was observed, and temperature trends differed slightly at mid power density levels. Upon unmounting the cell from its housing, it was immediately apparent that one of its four sections had detached from the rest of the device. Additionally, the mounting surface appeared significantly burned, as shown in Fig. 18. A second brand-new cell, identical to the previous one and referred to as Part 2, was characterized as a counter-evidence to validate the results

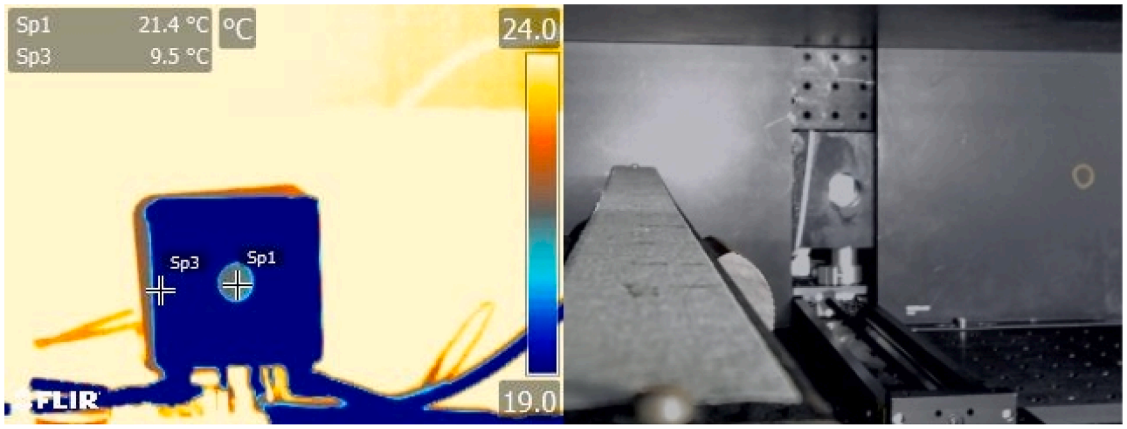


Fig. 16. Thermal camera (sx) and auxiliary camera (dx).

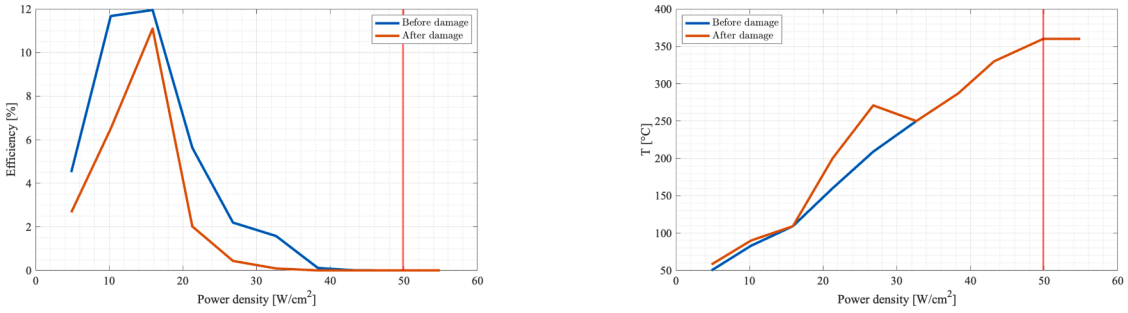


Fig. 17. **a** Efficiency of the cell during and after the damage test. **b** Temperature of the cell during and after the damage test.

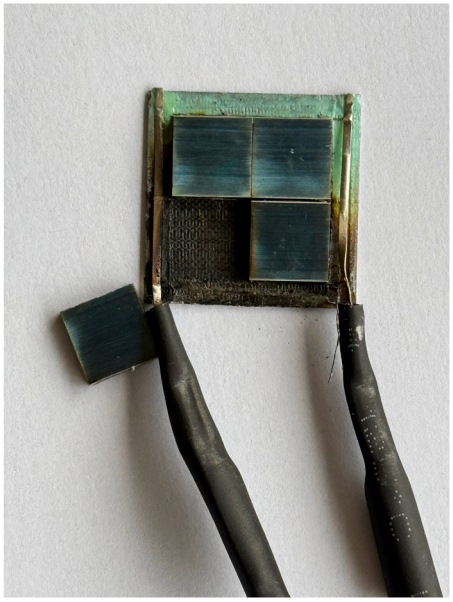
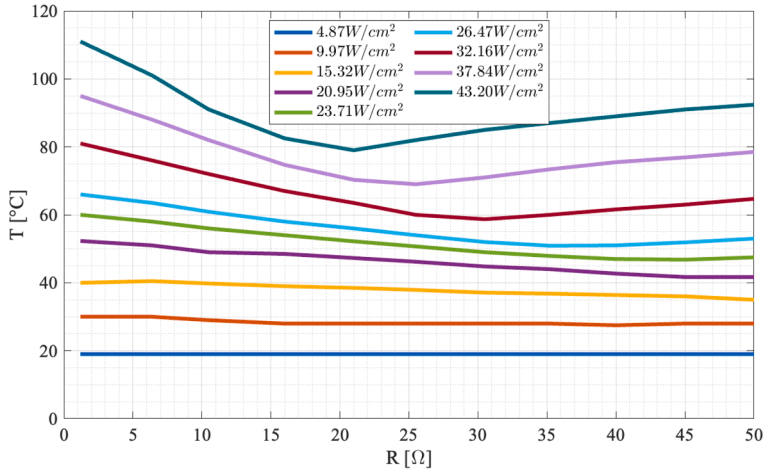
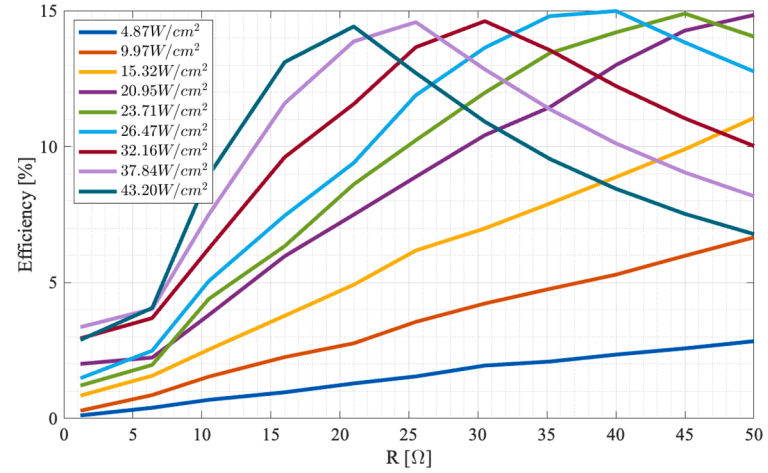


Fig. 18. Detail of the damaged part.

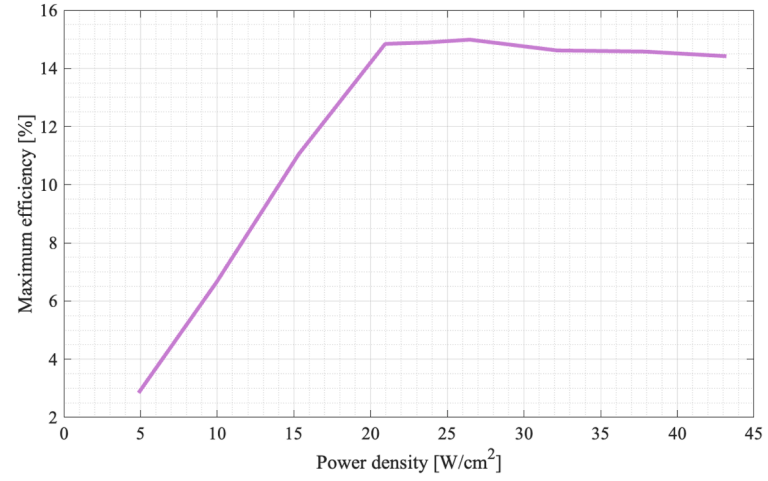
obtained from Part 1. On the basis of the damaging test results, the approach for this characterization was to increase the power density on the cell until there was an increase in efficiency while avoiding any damage or unnecessary stress to the sample. The first noticeable observation of this characterization was the significantly better thermal performance of Part 2 compared to Part 1, as shown in Fig. 19a. Regarding the efficiency trend of Part 2 (Fig. 19b), the maximum efficiency achieved was higher than that of Part 1, although still lower than the value declared in the data sheet. The best measured condition showed an efficiency of 14.62% with a power density of 26.47 [W/cm^2] and a load of 30[Ω]. Increasing the power density further resulted in a decrease in the cell's conversion efficiency, as clearly illustrated in Fig. 19c. During the characterization of part 2, the power density was increased up to a maximum of 43.2 [W/cm^2] without damaging the cell, likely due



(a)



(b)



(c)

Fig. 19. **a** Thermal behavior of Part 2. **b** Efficiency of Part 2 versus load in different power density conditions. **c** Maximum efficiency with optimal load of Part 2 for each power density level.

to its better thermal performance. The superior performance of part 2 could be attributed to the fact that it was a new device, never previously used or subjected to stress conditions. Alternatively, it may inherently possess a higher level of reliability and functionality compared to part 1.

9. Conclusions

Focusing on the satellite architecture, key subsystems, and experimental results related to the receiver, this paper contains an analysis of a laser-based wireless power transmission system designed for lunar appli-

cations. The design aims to address the challenges of the energy supply on the Moon, where traditional solar panel solutions are inefficient due to long lunar nights and permanently shadowed regions. Experimental tests were conducted on the photonic power converter and high-power laser system. These tests demonstrated the feasibility of converting laser energy into electrical power with notable efficiency. The best performing photonic power converters achieved conversion efficiencies of up to 16.3% in high-power density scenarios. Although these results fall slightly below theoretical expectations, they offer valuable insights into the practical performance of the system under operational conditions, and provide a solid foundation for future improvements in materials and design. Furthermore, the preliminary analysis conducted in this paper provides a first design of the satellite's geometries and attitude control system, which will play a critical role in maintaining precise laser pointing accuracy. This accuracy is essential to ensure efficient energy transmission from lunar orbit to the surface. Future work will include a more in-depth analysis of the satellite in all its components, focusing on the fiber laser design and the entire GNC system, including sensors and navigation algorithms. In addition, a power transmission test using a 1 [kW] fiber laser with a receiver 100 [m] away is planned.

CRediT authorship contribution statement

Domenico Edoardo Sfasciamuro: Writing – review & editing, Writing – original draft, Methodology, Investigation, Formal analysis, Conceptualization; **Catello Leonardo Matonti:** Writing – review & editing, Writing – original draft, Visualization, Supervision; **Francesco Lopez:** Writing – review & editing, Writing – original draft, Methodology, Formal analysis, Data curation, Conceptualization; **Anna Mauro:** Writing – review & editing, Writing – original draft, Methodology, Formal analysis, Data curation, Conceptualization; **Stefano Mauro:** Visualization, Supervision, Project administration, Funding acquisition, Conceptualization; **Andrea Villa:** Supervision, Project administration, Conceptualization.

Declaration of competing interest

The authors have declared no conflict of interest.

Acknowledgement

Manuscript presented at the International Astronautical Congress, IAC 2024, Milan, Italy, 14–18 October 2024. Copyright by IAF. This research was funded by ASI grant number DC-DSR-UVS-2022-375.

Data availability

Data will be made available on request.

References

[1] ESA, N°25–2023: Europe is aiming for the Moon, 2023, Available online: https://www.esa.int/Newsroom/Press_Releases/Europe_is_aiming_for_the_Moon [Accessed: February 21, 2024].
[2] Smart Lander for Investigating Moon (SLIM),J. A. E. Agency, 2023, Available online: https://global.jaxa.jp/projects/sas/slim/ [Accessed: February 20, 2024].
[3] Chandrayaan-3 is on its journey to the moon, 2023, Available online: https://www.isro.gov.in/Chandrayaan3_Details.html [Accessed: February 15, 2024].
[4] Global Exploration Roadmap, lunar surface exploration scenario update,I. S. E. C. Group, 2020, Available online: https://www.globalspaceexploration.org/wp-content/uploads/2020/08/GER_2020_supplement.pdf [Accessed: February 20, 2024].
[5] China-Russia space Cooperation: The strategic, military, diplomatic, and economic implications of a growing relationship,C. A. S. Institute, 2023, Available online: https://www.cna.org/reports/2023/06/china-russia-space-cooperation-may-2023 [Accessed: January 20, 2024].
[6] NASA, Lunar reconnaissance orbiter: permanently shadowed regions on the moon, 2023, Available online: https://science.nasa.gov/wp-content/uploads/2024/01/lro-litho5-shadowed.pdf [Accessed: January 10, 2024].
[7] NASA, VIPER - volatiles investigating polar exploration rover, 2024, Available online: https://science.nasa.gov/mission/viper/ [Accessed: February 5, 2024].
[8] NASA, VIPER - mission timeline, 2024, Available online: https://science.nasa.gov/mission/viper/in-depth/ [Accessed: February 20, 2024].
[9] K. Jin, W. Zhou, Wireless laser power transmission: a review of recent progress, IEEE Trans. Power Electron. 34 (4) (2019) 3842–3859. https://doi.org/10.1109/TPEL.2018.2853156
[10] L. Summerer, O. Purcell, Concepts for wireless energy transmission via laser, in: International Conference on Space Optical Systems and Applications (ICSOS), 2009.
[11] T. He, G. Zheng, Q. Wu, H. Huang, L. Wan, K. Xu, T. Shi, Z. Lv, Analysis and experiment of laser energy distribution of laser wireless power transmission based on a powersphere receiver, Photonics 10 (7) (2023). https://doi.org/10.3390/photonics10070844
[12] A. Mohammadnia, B.M. Ziapour, H. Ghaebi, M.H. Khooban, Feasibility assessment of next-generation drones powering by laser-based wireless power transfer, Opt. Laser Technol. 143 (2021) 107283. https://doi.org/10.1016/j.optlastec.2021.107283
[13] M.-A. Lahmeri, M.A. Kishk, M.-S. Alouini, Laser-powered UAVs for wireless communication coverage: a large-scale deployment strategy, IEEE Trans. Wirel. Commun. 22 (1) (2023) 518–533. https://doi.org/10.1109/TWC.2022.3195867
[14] F. Lopez, A. Mauro, S. Mauro, G. Monteleone, D.E. Sfasciamuro, A. Villa, A lunar-orbiting satellite constellation for wireless energy supply, Aerospace 10 (11) (2023). https://doi.org/10.3390/aerospace10110919
[15] F. Lopez, A. Mauro, D.E. Sfasciamuro, A. Villa, S. Mauro, Wireless power transmission: a new frontier for lunar colonisation development, in: 2024 11th International Workshop on Metrology for AeroSpace (MetroAeroSpace), 2024, pp. 303–308. https://doi.org/10.1109/MetroAeroSpace61015.2024.10591567
[16] M. Beattie, H. Helmers, G. Forcade, C. Valdivia, O. Höhn, K. Hinzer, InP- and GaAs-based photonic power converters under O-band laser illumination: performance analysis and comparison, IEEE J. Photovolt. PP (2022) 1–9. https://doi.org/10.1109/JPHOTOV.2022.3218938
[17] C. Algora, I. García, M. Delgado, R. Peña, C. Vázquez, M. Hinojosa, I. Rey-Stolle, Beaming power: photovoltaic laser power converters for power-by-light, Joule 6 (2) (2022) 340–368. https://doi.org/10.1016/j.joule.2021.11.014
[18] A. Tünnermann, T. Schreiber, J. Limpert, Fiber lasers and amplifiers: an ultrafast performance evolution, Appl. Opt. 49 (2010) F71–8. https://doi.org/10.1364/AO.49.000F71
[19] J. Limpert, F. Roeser, S. Klingebiel, T. Schreiber, C. Wirth, T. Peschel, R. Eberhardt, A. Tiinnermann, The rising power of fiber lasers and amplifiers, Sel. Top. Quantum Electron. IEEE J. OF 13 (2007) 537–545. https://doi.org/10.1109/JSTQE.2007.897182
[20] M.N. Ott, W.J. Thoma, F.V. LaRocca, R.F. Chuska, R. Switzer, L. Day, Optical fiber assemblies for space flight from the NASA goddard space flight center, photonics group, in: International Symposium on Reliability of Optoelectronics for Space (ISROS), 2009.
[21] A. Yu, M. Krainak, M. Stephen, J. Chen, D. Coyle, K. Numata, J. Camp, J. Abshire, G. Allan, S. Li, H. Riris, Fiber lasers and amplifiers for space-based science and exploration, Prog. Biomed. Opt. Imaging Proc. SPIE 8237 (2012) 23. https://doi.org/10.1117/12.916069
[22] N. Yu, J. Ballato, M.J.F. Digonnet, P.D. Dragic, Optically managing thermal energy in high-power Yb-doped fiber lasers and amplifiers: a brief review, Curr. Opt. Photon. 6 (6) (2022) 521–549. https://doi.org/10.3807/COPP.2022.6.6.521
[23] J.H.S J. Csank, Power and energy for the lunar surface, in: Advanced Research Projects Agency-Energy (ARPA-E) Tech-to-Market Team, 2022.
[24] J. Csank, NASA Lunar surface operations & power grid, in: 11th Annual Center for Ultra-Wide-Area Resilient Electric Energy Transmission Networks (CURENT) Industry Conference, 2023.
[25] J.W. Goodman, Introduction to Fourier Optics, McGraw-Hill physical and quantum electronics series, W. H. Freeman, 2005.
[26] I. P. Corp, High-power fiber lasers, Avalaible online at: https://www.ipgphotonics.com/products/lasers/industrial-cw-fiber-lasers/high-power-fiber-lasers#ftrre-sources.
[27] M. Serkan, H. Kirkici, H. Cetinkaya, Off-axis mirror based optical system design for circularization, collimation, and expansion of elliptical laser beams, Appl. Opt. 46 (2007) 5489–5499. https://doi.org/10.1364/AO.46.005489
[28] K. Ferrone, C. Willis, F. Guan, J. Ma, L. Peterson, S. Kry, A review of magnetic shielding technology for space radiation, Radiation 3 (1) (2023) 46–57. https://doi.org/10.3390/radiation3010005
[29] G. Reitz, T. Berger, D. Matthiae, Radiation exposure in the moon environment, Planet. Space Sci. 74 (1) (2012) 78–83. Scientific Preparations For Lunar Exploration. https://doi.org/10.1016/j.pss.2012.07.014
[30] S. Vadawale, J. Goswami, T. Dachev, B. Tomov, V. Girish, Radiation environment in earth-moon space: results from RADOM experiment onboard chandrayaan-1 25 (2010). https://doi.org/10.1142/9789814355377_0009
[31] J. Grandidier, P. Jaffe, W. Roberts, M. Wright, A. Fraeman, C. Raymond, A. Austin, P. Lubin, E. Sunada, J.-P. Jones, A. Barchowsky, J. Baker, Laser power beaming for lunar night and permanently shadowed regions, Bull. AAS 53 (2021). https://doi.org/10.3847/25c2cfeb.13f46900
[32] J. Grandidier, P. Jaffe, W.T. Roberts, M.W. Wright, A.A. Fraeman, C.A. Raymond, A. Austin, P. Lubin, E.T. Sunada, J.-P. Jones, A. Barchowsky, J.D. Baker, Laser power beaming for lunar night and permanently shadowed regions, in: Bulletin of the American Astronomical Society, 53, 2021, p. 302. https://doi.org/10.3847/25c2cfeb.13f46900
[33] E. Spreen, K. Howell, D. Davis, NEAR RECTILINEAR HALO ORBITS AND THEIR APPLICATION IN CIS-LUNAR SPACE, in: 3rd IAA Conference on Dynamics and Controls of Space Systems, 2017.
[34] Z.-Y. Gao, X.-Y. Hou, Coverage analysis of lunar communication/navigation constellations based on halo orbits and distant retrograde orbits, J. Navig. 73 (4) (2020) 932–952. https://doi.org/10.1017/S0373463320000065

[35] R. Whitley, D. Davis, L. Burke, B. McCarthy, R. Power, M. McGuire, K. Howell, Earth-moon near rectilinear halo and butterfly orbits for lunar surface exploration, in: AAS/AIAA Astrodynamics Specialist Conference, 2018.
[36] A. Villa, Astrodynamics and Analysis of Lunar Space-Based Solar Power Missions, Master's thesis, Politecnico di Torino, 2025.
[37] A. Rivolta, A. Colagrossi, V. Pesce, S. Silvestrini, Chapter five - Attitude dynamics, in: V. Pesce, A. Colagrossi, S. Silvestrini (Eds.), Modern Spacecraft Guidance, Navigation, and Control, Elsevier, 2023, pp. 207–252. https://doi.org/10.1016/B978-0-323-90916-7.00005-6
[38] B. Wie, P. Barba, Quaternion feedback for spacecraft large angle maneuvers. AIAA J. Guid. Control Dyn. 8, 360–365, J. Guid. Contr. Dyn. J Guid Contr. Dynam 8 (1985) 360–365. https://doi.org/10.2514/3.19988
[39] J.-H. Lee, D. Kim, J. Kim, H.-S. Oh, Shorter path design and control for an underactuated satellite, Int. J. Aerosp. Eng. 2017 (2017) 1–9. https://doi.org/10.1155/2017/8536732
[40] D. Xia, Detailed Balance Modeling of Monochromatic Photovoltaic Power Conversion, Master's thesis, University of Ottawa, 2020.
[41] H. Helmers, E. Lopez, O. Höhn, D. Lackner, J. Schön, M. Schauerte, M. Schachtner, F. Dimroth, A.W. Bett, Pushing the boundaries of photovoltaic light to electricity conversion: a GaAs based photonic power converter with 68.9% efficiency, in: 2021 IEEE 48th Photovoltaic Specialists Conference (PVSC), 2021, pp. 2286–2289. https://doi.org/10.1109/PVSC43889.2021.9518920
[42] N.A. Kalyuzhnyy, A.V. Malevskaya, S.A. Mintairov, M.A. Mintairov, M.V. Nakhimovich, R.A. Salii, M.Z. Shvarts, V.M. Andreev, Photovoltaic AlGaAs/GaAs devices for conversion of high-power density laser (800–860 nm) radiation, Sol. Energy Mater. Sol. Cells 262 (2023) 112551. https://doi.org/10.1016/j.solmat.2023.112551
[43] M. Green, Limiting photovoltaic monochromatic light conversion efficiency, Prog. Photovolt. Res. Appl. 9 (2001) 257–261. https://doi.org/10.1002/pip.375
[44] D. Xia, M.M. Wilkins, S.S. viperhal, C.E. Valdivia, K. Hinzer, J.J. Krich, Opportunities for increased efficiency in monochromatic photovoltaic light conversion, in: 2018 IEEE 7th World Conference on Photovoltaic Energy Conversion (WCPEC) (a Joint Conference of 45Th IEEE PVSC, 28th PVSEC and 34th EU PVSEC), 2018, pp. 3688–3692. https://doi.org/10.1109/PVSC.2018.8547912
[45] N.A. Kalyuzhnyy, V.M. Emelyanov, S.A. Mintairov, M.V. Nahimovich, R.A. Salii, M.Z. Shvarts, InGaAs metamorphic laser power converters with distributed bragg reflector for wavelength range $\lambda = 1 - -1.1\mu m$, AIP Conf. Proc. 2298 (1) (2020) 030001. https://doi.org/10.1063/5.0032903
[46] D.S. Simon, Gaussian beams and lasers, in: A Guided Tour of Light Beams, 2053–2571, Morgan & Claypool Publishers, 2016, pp. 3–1 to 3–14. https://doi.org/10.1088/978-1-6817-4437-7ch3